

## NUCLEAR CORE-QUASIPARTICLE COUPLING

S. E. LARSSON, G. LEANDER <sup>†</sup> and I. RAGNARSSON <sup>††</sup>

*Department of Mathematical Physics, Lund Institute of Technology, Lund, Sweden*

Received 3 May 1978

(Revised 21 June 1978)

**Abstract:** Relations between different core-particle coupling models based on the Bohr Hamiltonian are discussed, and in particular the  $\gamma$ -unstable and rigid  $30^\circ$  triaxial cores are compared quantitatively. A new formulation is developed employing a rigid triaxial rotor core and the strong-coupling basis. Within the limitations imposed by this model core, it is equally applicable in the limits of small and extremely large deformations. Sample calculations are made for the nuclei  $^{185}\text{Re}$  and  $^{75,77}\text{Se}$ . The results for the latter support earlier predictions of an oblate-prolate shape transition in this region of nuclei, but also indicate difficulties in the treatment of pairing. As another application, the wave functions and excitation energies of decoupled states are illuminated from the point of view of the strong-coupling basis, and the effects of hexadecapole deformation and  $j$ -mixing are examined.

### 1. Introduction

In 1952 Bohr <sup>1)</sup> tentatively suggested that the many-body Hamiltonian of an odd-mass nuclear system can be approximated by

$$H = H_{\text{core}}(\alpha) + H_{\text{part}}^{\bar{\alpha}} + H_{\text{int}}(\alpha), \quad (1)$$

where  $\alpha$  stands for the collective coordinates of the core. Here  $H_{\text{core}}(\alpha)$  is a collective Hamiltonian for the doubly even core,  $H_{\text{part}}^{\bar{\alpha}}$  is the single-particle Hamiltonian in an adiabatic core field corresponding to some fixed set  $\bar{\alpha}$  of the collective coordinates, and  $H_{\text{int}}$  takes into account the effect on the odd particle of that part of the core field which is not already included in  $H_{\text{part}}^{\bar{\alpha}}$ . This approach was first applied by Bohr and Mottelson <sup>2)</sup> and subsequently by many others. It has turned out that in this way a great deal of information concerning shell-model parameters, core deformations and other important features of nuclear structure can be extracted from the experimental data on odd-mass nuclei. Recent developments of experimental techniques, particularly in the field of heavy-ion reactions, are presently leading to a considerable extension of available data on odd- $A$  spectra and thereby providing new impetus for such analyses. The work of Meyer-ter-Vehn <sup>3)</sup> has established the important role of non-axial shape degrees of freedom in the core <sup>4,5)</sup>, and several generalized approaches have been developed which take this into account <sup>6–8)</sup>. In all of these  $\bar{\alpha}$  is

<sup>†</sup> Present address: NORDITA, Copenhagen, Denmark.

<sup>††</sup> Present address: CERN, Geneva, Switzerland.

chosen to correspond to a spherical shape. However, in practical calculations it is necessary to severely truncate the single-particle space spanned by the eigenstates of  $H_{\text{part}}^{\bar{\alpha}}$ , and only one or a few  $j$ -shells can be retained. However, if the average core field is deformed the truncation effects will be less serious if  $\bar{\alpha}$  is chosen accordingly. This leads us to take a deformed shell-model single-particle Hamiltonian <sup>9)</sup>, which in earlier work has been applied to core-particle coupling only under the restrictive assumptions of adiabaticity <sup>10)</sup>, axial symmetry <sup>11)</sup> or small vibrations around axial symmetry <sup>12)</sup>.

In the model of Hecht and Satchler <sup>10)</sup> an odd particle occupying a deformed single-particle orbital is coupled to a rigid triaxial rotor core. The present paper describes a generalization whose essence is to increase the number of deformed orbitals available to the odd particle until convergence is obtained. Thereby the adiabatic approximation is removed. The strong-coupling basis <sup>1)</sup> is still used, but this is a technical device to ensure rapid convergence at any deformation. In the limit of small deformations the present model is equivalent e.g. to the model of Meyer-ter-Vehn <sup>3)</sup>.

## 2. The model

### 2.1. THE HAMILTONIAN

Let us recall how the particle-rotor Hamiltonian is obtained from the general Bohr Hamiltonian (1). It is assumed that the core field acting on the odd particle is determined by the core collective variables through some prescription satisfying the requirement of rotational invariance, for example

$$V(\alpha, r) = U(r^2 \{1 + \sum_{\lambda} [\alpha_{\lambda} \times Y_{\lambda}(\Omega_p)]^0 + O(\alpha^2)\}). \quad (2)$$

This total potential can be expanded in a Taylor series around a static field defined by  $\bar{\alpha}$ , and the zero-order term goes into  $H_{\text{part}}^{\bar{\alpha}}$  while the remaining terms constitute  $H_{\text{int}}(\alpha)$ . For example, choosing  $\bar{\alpha} = 0$  gives to first order in  $\alpha$

$$H = H_{\text{core}}(\alpha) + H_{\text{part}}^{\bar{\alpha}=0} + r^2 \frac{dU(r^2)}{dr^2} \sum_{\lambda} [\alpha_{\lambda} \times Y_{\lambda}]^0, \quad (3)$$

where the potential in  $H_{\text{part}}^{\bar{\alpha}=0}$  is  $U(r^2)$ . This is the intermediate coupling Hamiltonian. In principle its only limitation relative to the full Hamiltonian (1) lies in the neglect of second- and higher-order terms in  $\alpha$ . In practice another difficulty arises when the first-order term in  $\alpha$  is more than a small perturbation, namely that the size of the single-particle basis required for numerical convergence may be unmanageably large.

In this respect it is better to expand around a value  $\bar{\alpha}$  which in some sense corresponds to the static average of the core field and minimizes  $H_{\text{int}}(\alpha)$ . Since there is isotropy with regard to the spatial orientation of the nucleus, this can be achieved

only for the intrinsic coordinates of  $\alpha$ . In the intrinsic frame of reference the potential (2) is

$$V(\alpha, r) = U(r^2 \{1 - e \cos \gamma Y_2^0(\Omega_p) + \sqrt{\frac{1}{2}} e \sin \gamma (Y_2^2(\Omega_p) + Y_2^{-2}(\Omega_p)) + \dots\}), \quad (4)$$

and the zero-order term from an expansion around  $\bar{\alpha} = \bar{e}, \bar{\gamma}, \dots$  gives a deformed shell model potential <sup>9</sup>), whose eigenstates can be used for the single-particle basis. In the present work all but this zero-order term will be neglected, so that the vibrational part of  $H_{\text{int}}(\alpha)$  disappears completely. This is the rigid core approximation, which will be examined in the next section. With the intrinsic part of  $\alpha$  frozen, only the orientation coordinates remain as dynamical variables and the Hamiltonian (1) reduces to

$$H = \sum_{\kappa=1}^3 R_{\kappa}^2(\theta_i)/2J_{\kappa} + H_{\text{part} + \text{int}}^{\bar{e}, \bar{\gamma}, \dots}(\theta_i), \quad (5)$$

where  $R$  is the angular momentum of the core,  $\kappa$  refers to the intrinsic axes and  $J_{\kappa}$  are the constant moments of inertia. The particle-rotation coupling is marked as being present in the second term of (5) because the single-particle wave functions do not refer to the lab frame but to the intrinsic frame defined by the core. However, when diagonalizing in basis states that are not themselves eigenstates of the first term in (5), it is possible to choose them in such a way that the contributions from the particle-rotation interaction in the second term of (5) are transformed away. This choice is the strong-coupling basis. Then  $R$  is most conveniently expressed as the difference between the total angular momentum  $I$  and the single-particle contribution  $j$ , and the Hamiltonian (5) becomes

$$H = \sum_{\kappa=1}^3 (I_{\kappa}^2(\theta_i) - 2I_{\kappa}(\theta_i)j_{\kappa} + j_{\kappa}^2)/2J_{\kappa} + H_{\text{part}}^{\bar{\alpha}}, \quad (6)$$

Here the particle-rotation interaction has been transformed into  $H_{\text{core}}$  instead, and emerges in the form of a Coriolis term  $-\sum I_{\kappa}j_{\kappa}/J_{\kappa}$  and a recoil term  $\sum j_{\kappa}^2/2J_{\kappa}$ .

To the extent that  $j_{\kappa}^2$  can be treated as a single-particle term, it could in principle be absorbed in  $H_{\text{part}}^{\bar{\alpha}}$ . However, it would be correct to delete the recoil term from (6) only if the deformed shell model contained such a term explicitly <sup>13</sup>).

## 2.2. THE RIGID CORE APPROXIMATION

The concept of a rigid core shape cannot be taken literally. Obviously, no function of the single-particle coordinates that is used to define a deformation can be a conserved quantity, because it does not commute with a microscopic Hamiltonian containing derivatives with regard to the particle coordinates.

An estimate of the lower limit to the shape vibrational amplitude can be taken from a shell-model evaluation of the uncertainty in the quadrupole components  $Q_{20}$  and  $Q_{22}$ , i.e. the zero-point vibrational amplitude of the giant quadrupole mode. The

standard deviation for  $Q_{20}$  converted to  $\beta$ -deformation is

$$\sigma(\beta) \approx \begin{cases} 0.10, & A \approx 100 \\ 0.05, & A \approx 200, \end{cases}$$

and a corresponding amount for  $Q_{22}$  and  $\gamma$ -deformation. In transitional nuclei this is a sizeable fraction of the total deformation.

The essence of the rigid core approximation leading to the Hamiltonian (6) can be understood from inspection of the intermediate coupling variant (3) of the Bohr Hamiltonian. There it is clear that the core properties influence the odd- $A$  spectrum through (i) the energies of the excited core states and (ii) the reduced multipole matrix elements between these states. These two sets of quantities can be referred to as the total multipole field of the core, and the rigid rotor can be viewed as a few-parameter family of multipole fields which is useful to the extent that it can be adjusted to reproduce the essential features of the nuclear multipole field. The parameters are the intrinsic multipole moments  $Q_{\lambda\mu}$  and the three rotational moments of inertia  $J_\kappa$ ,  $\kappa = 1, 2, 3$ . However, in the present paper we will not exhaust the possibilities of the family since the formal developments of the next section require all parity-breaking multipole moments to be zero, and furthermore in the applied calculations the three moments of inertia are assumed to be connected by a relationship of hydrodynamical type,

$$J_\kappa = \frac{4}{3}J_0 \sin^2(\gamma + \kappa\frac{2}{3}\pi). \quad (7)$$

In order to get some insight into the differences between the multipole fields of rigid and dynamical cores, let us study the quadrupole mode. In the case of a nucleus with stable axial symmetry it is well known that the effect of vibrations on the ground and  $\gamma$  bands are simulated by a rigid rotor with a small "effective"  $\gamma$ . The quadrupole matrix elements can be closely reproduced<sup>14)</sup>. The vibrational bands, completely absent in the rigid rotor, couple only weakly to these two bands. In the following we proceed to compare the rigid rotor with solutions of the Bohr Hamiltonian in the soft collective potentials believed to be characteristic of transitional nuclei. *A priori* one might suspect that isotropy with regard to  $\gamma$  could be important for the odd- $A$  spectrum, in analogy with the isotropy with regard to the spatial orientation angles giving rise to the Coriolis force.

Fig. 1 shows results obtained with the intermediate coupling Hamiltonian (3). A  $j = \frac{3}{2}$  particle is coupled to schematic cores whose excitation spectra include only the ground and  $\gamma$  bands up to spin 10. Their mass functions have the hydrodynamical functional form and their parameters are typical for a transitional nucleus in the  $A = 190$  mass region. The label " $\gamma$ -unstable" refers to the solution of the Bohr Hamiltonian in a  $\beta$ -deformed but  $\gamma$ -unstable potential. The  $\beta$ -deformation is so stiff that the  $\beta$ -vibrational  $0^+$  band head has an excitation energy about 1.5 times greater than that of the seniority-3  $\gamma$ -vibrational  $0^+$  state. In the case of the "dynamical rotor"

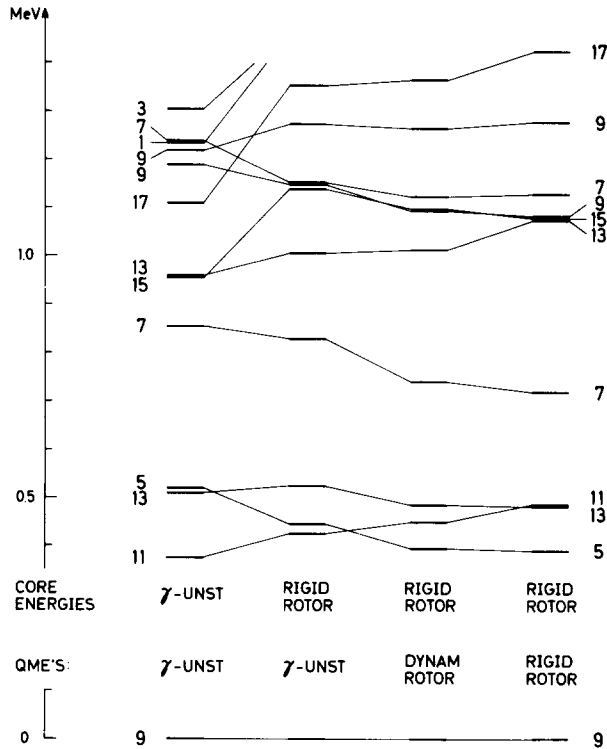


Fig. 1. The " $j = \frac{3}{2}$  spectra" resulting from intermediate coupling calculations with different core parameters. The core parameters are evaluated for three different cases, namely (i) a  $\gamma$ -unstable but  $\beta$ -deformed potential ( $\gamma$ -unst), (ii) a potential with a minimum at  $\gamma = 30^\circ$  (dynam rotor) and (iii) a rigid rotor at  $\gamma = 30^\circ$  (rigid rotor). The core quantities which enter in the odd- $A$  spectra are the energies of the excited core states and the reduced matrix elements between these states (see eq. (3)). Different combinations of these quantities are shown in the different spectra. In all cases only the ground and  $\gamma$ -bands up to spin 10 are included. Note that except for the decreased stiffness of the core rotational bands when the rigid core approximation is removed, the  $j = \frac{3}{2}$  spectrum is not very much affected by the exhibited changes in core properties. The following parameters are the same in all four cases: The excitation energy of the first  $2^+$  state,  $E(2^+) = 0.358$  MeV, the quadrupole matrix element between this state and the ground state  $B(E2; 2^+ \rightarrow 0^+) = 0.419 e^2 \cdot b^2$ , the particle-core coupling constant,  $k = 40$  MeV, the mass number,  $A = 193$  and the proton number,  $Z = 79$ .

the Bohr Hamiltonian has been solved in a potential whose minimum in the  $\beta$ -direction is 4 MeV deeper at  $\gamma = 30^\circ$  than at  $\gamma = 0^\circ$  and  $60^\circ$ . The  $\gamma = 30^\circ$  "rigid rotor" is chosen to have the same excitation energy and quadrupole matrix element from the ground state to the lowest  $2^+$  state as was calculated in the " $\gamma$ -unstable" case.

The first two spectra of fig. 1 show the effect of changing the core energies. The increased stiffness of the core rotational bands when the rotation-vibration interaction is removed is straightforwardly reflected in the odd- $A$  spectrum. This is a major drawback of the rigid core approximation. It can be circumvented by means of

a variable moment of inertia <sup>15</sup>), which, however, is tedious to implement when the strong-coupling basis is used. The three right-hand spectra exhibit the effects of changes in the quadrupole matrix elements. Only small shifts of the odd-*A* levels occur, and they can be interpreted to reflect the polarizability of the  $\gamma$ -unstable core. If the  $\gamma$ -deformation of the equivalent rotor core had been chosen slightly in excess of 30°, the shifts would have been even smaller. A few of the core quadrupole matrix elements are given in table 1. One systematic difference arises from centrifugal

TABLE 1

Some reduced quadrupole matrix elements for the three model cores referred to in figs. 1 and 2

Transition	$\gamma$ -unstable	Dynam. rotor	Rigid rotor
<i>ground <math>\rightarrow</math> ground band</i>			
2 $\rightarrow$ 0	-100	-100	-100
4 $\rightarrow$ 2	-165	-164	-158
6 $\rightarrow$ 4	-222	-222	-212
8 $\rightarrow$ 6	-275	-274	-255
<i><math>\gamma \rightarrow \gamma</math> band</i>			
3 $\rightarrow$ 2	138	157	158
4 $\rightarrow$ 2	-134	-117	-104
5 $\rightarrow$ 3	-160	-156	-145
5 $\rightarrow$ 4	108	139	145
6 $\rightarrow$ 4	199	176	138
<i><math>\gamma \rightarrow</math> ground band</i>			
2 $\rightarrow$ 2	123	122	120
3 $\rightarrow$ 4	87	105	118
4 $\rightarrow$ 4	127	102	70
5 $\rightarrow$ 6	108	122	126
6 $\rightarrow$ 6	-136	-100	-61
<i>higher <math>\gamma \rightarrow \gamma</math> band</i>			
0 $\rightarrow$ 2	-62	-34	
2 $\rightarrow$ 3	101	59	
2 $\rightarrow$ 4	-62	-42	
4 $\rightarrow$ 4	-136	-167	-178
4 $\rightarrow$ 3	-146	-128	-100
<i>higher <math>\gamma \rightarrow</math> ground band</i>			
2 $\rightarrow$ 2	0	12	
4 $\rightarrow$ 2	0	12	27
<i><math>\beta \rightarrow</math> ground band</i>			
0 $\rightarrow$ 2	27	24	
2 $\rightarrow$ 0	-12	-12	
2 $\rightarrow$ 4	-46	-41	
<i><math>\beta \rightarrow \gamma</math> band</i>			
2 $\rightarrow$ 2	34	31	

The matrix elements are scaled so that  $\langle 0_1 || Q || 2_1 \rangle = -100$ , and the phases are consistent but not unique. In all three cases, many matrix elements are zero as a consequence of the  $\gamma$ -parity selection rule <sup>16</sup>). Notably all the diagonal ones belong to this category.

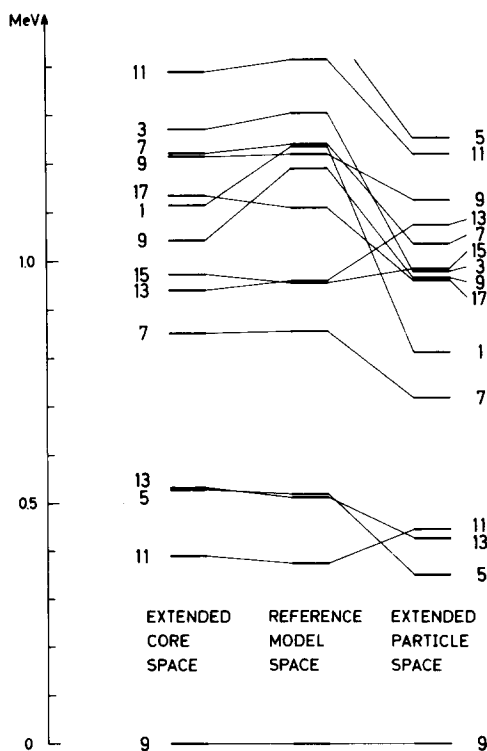


Fig. 2. The " $j = \frac{9}{2}$  spectra" resulting from intermediate coupling calculations with different truncation of the basis spaces. The middle spectrum is identical with the left-hand spectrum of fig. 1 and is thus calculated from a  $\gamma$ -unstable potential. The single-particle basis space is restricted to the  $h_{9/2}$  shell and for the core states only the ground and  $\gamma$ -bands up to spin 10 are considered. In the spectrum to the left, the ten additional core states of lowest energy are included while in the spectrum to the right the  $f_{7/2}$  and  $f_{5/2}$  shells placed at realistic energies for the  $A = 190$  region have been included in the single-particle space. Note that the truncation of the particle space appears to be much more severe than the truncation of the core space.

stretching of the dynamical cores. Another is that the  $\gamma$  to ground band matrix elements are largest from odd-spin states in the rigid rotor, while in the  $\gamma$ -unstable core they are largest from the even-spin  $\gamma$ -band members. Currently attempts are being made to analyze Coulomb excitation yields from doubly even nuclei in terms of these differences<sup>17)</sup>.

The spectrum in the middle of fig. 2 is the same as that to the left in fig. 1. The left-hand spectrum of fig. 2 shows the effect of including the ten additional states of lowest energy in the schematic core space of the coupling calculation. These higher-lying vibrational states, most of which do not have analogs in the rigid rotor, clearly do not affect the yrast states of an odd- $A$  nucleus, the reason being that they couple weakly or not at all to the yrast states of the core. On the other hand the energy of the  $\frac{9}{2}_2$  state changes a little, because its wave function has a large contribution from the  $2^+_{\frac{1}{2}}$  core state which couples to the  $\gamma$ -vibrational  $0^+$  state (table 1).

In order to put perspective on the size of the shifts in figs. 1 and 2, the right-hand spectrum of fig. 2 shows the effect of including a few additional  $j$ -shells in the intermediate coupling calculation. They are the  $f_{7/2}$  and  $f_{5/2}$  shells, placed at 1 and 3.5 MeV, respectively above the  $h_{9/2}$  shell. These spacings are realistic for protons in the  $A \approx 190$  mass region. It is the effect of these and all other relevant shells that can be fully taken into account by using the strong-coupled basis, the price to be paid being the rigid core approximation. However, the tentative conclusion to be drawn from the calculations in this section and in refs. <sup>7,8</sup>) is that the core parameters which are most relevant for the odd- $A$  spectrum are precisely the effective intrinsic moments entering the rigid rotor model, while large-amplitude fluctuations around these values affect only weakly the levels that are most likely to be observed experimentally.

As mentioned above, discrepancies will arise when the rigid rotor rotational bands are "too stiff". However, also the full dynamical theory is incapable of reproducing "upbending" or "backbending" effects in the yrast line, caused by the rotational alignment of core particles with high  $j$ -values. In the Alaga model <sup>18</sup>) this mechanism is taken into account by abstracting an appropriately chosen two-particle cluster from the core and including it in  $H_{\text{part}}$  of eq. (1). A lucid example is the calculation for  $^{54}\text{Fe}_{28}$  in ref. <sup>19</sup>). For the future it may be worthwhile to investigate whether the same end can be achieved by including a small number of three-quasiparticle configurations in the strong-coupled single-particle basis space.

### 2.3. METHOD OF CALCULATION

The following is a description of the method used in the applications of later sections for diagonalizing the triaxial core plus particle Hamiltonian (6) in the strong-coupling basis. First a single-particle model is employed to calculate the adiabatic energies  $\varepsilon_v$  and the wave functions  $\chi_v$  as expansions,

$$\chi_v = \sum_{\alpha j \Omega} c_{\alpha j \Omega}^{(v)} \psi_{\Omega}^{\alpha j}, \quad \alpha = N, l. \quad (8)$$

Here,  $\Omega$  is the projection of the single-particle angular momentum  $j$  along any one of the three principal axes, henceforth denoted as the 3-axis. With reflection symmetry, the time-reversal degeneracy can be exploited by restricting  $\Omega$  to the values  $\dots -\frac{3}{2}, \frac{1}{2}, \frac{5}{2}, \dots$ . The remaining  $\Omega$ -values then enter through the conjugate states

$$\tilde{\chi}_v = \sum_{\alpha j \Omega} (-)^{j-\Omega} c_{\alpha j \Omega}^{(v)} \psi_{-\Omega}^{\alpha j}. \quad (9)$$

Next it is necessary to select a few states  $\chi_v$  near the Fermi surface which may constitute an adequate truncated single-particle basis space for the non-adiabatic part of the calculation. The question of convergence has been examined in preliminary investigations of the model <sup>20</sup>); we will not dwell on it here and merely state the result that three or four single-particle orbitals of each parity is generally sufficient for the



purpose of studying states reasonably close to the yrast line. Having chosen the single-particle orbitals, one must then determine the matrix elements between them of the single-particle operators entering the Coriolis and recoil terms. When the Hamiltonian (6) is expressed in step operators

$$H = \frac{1}{4} \left( \frac{1}{J_1} + \frac{1}{J_2} \right) [I^2 - I_3^2 + j^2 - j_3^2 - (I_+ j_- + I_- j_+)] \\ + \frac{1}{8} \left( \frac{1}{J_1} - \frac{1}{J_2} \right) (I_+^2 + I_-^2 + j_+^2 + j_-^2 - 2(I_+ j_+ + I_- j_-)) + \frac{1}{2J_3} (I_3 - j_3)^2 + \sum_v \delta_{\mu\nu} \varepsilon_v, \quad (10)$$

it is seen that the required matrix elements are

$$(a+b)_{\mu\nu} = \langle \chi_\mu | j_+ | \tilde{\chi}_\nu \rangle = \sum_{\alpha j \Omega} c_{\alpha j \Omega}^{(\mu)} c_{\alpha j, -(\Omega-1)}^{(\nu)} (-)^{j-\Omega} \sqrt{j(j+1) - \Omega(\Omega-1)}, \quad (11)$$

$$c_{\mu\nu} = \langle \chi_\mu | j_- | \tilde{\chi}_\nu \rangle = \sum_{\alpha j \Omega} c_{\alpha j \Omega}^{(\mu)} c_{\alpha j, -(\Omega+1)}^{(\nu)} (-)^{j-\Omega} \sqrt{j(j+1) - \Omega(\Omega+1)}, \quad (12)$$

$$d_{\mu\nu} = \langle \chi_\mu | j^2 - j_3^2 | \chi_\nu \rangle = \sum_{\alpha j \Omega} c_{\alpha j \Omega}^{(\mu)} c_{\alpha j \Omega}^{(\nu)} (j(j+1) - \Omega^2), \quad (13)$$

$$e_{\mu\nu} = \langle \chi_\mu | j_+^2 + j_-^2 | \chi_\nu \rangle = \sum_{\alpha j \Omega} (c_{\alpha j \Omega}^{(\mu)} c_{\alpha j, \Omega-2}^{(\nu)} + c_{\alpha j, \Omega-2}^{(\mu)} c_{\alpha j \Omega}^{(\nu)}) \sqrt{j(j+1) - \Omega(\Omega-1)} \\ \times \sqrt{j(j+1) - (\Omega-1)(\Omega-2)}, \quad (14)$$

$$\langle \Omega \rangle_{\mu\nu} = \langle \chi_\mu | j_3 | \chi_\nu \rangle = \sum_{\alpha j \Omega} c_{\alpha j \Omega}^{(\mu)} c_{\alpha j \Omega}^{(\nu)} \Omega, \quad (15)$$

$$\langle \Omega^2 \rangle_{\mu\nu} = \langle \chi_\mu | j_3^2 | \chi_\nu \rangle = \sum_{\alpha j \Omega} c_{\alpha j \Omega}^{(\mu)} c_{\alpha j \Omega}^{(\nu)} \Omega^2. \quad (16)$$

Hecht and Satchler refer to them as generalized decoupling factors, because the first one contains as a special case the familiar decoupling factor for  $K = \frac{1}{2}$  bands <sup>21</sup>.

Note that the single-particle potential influences the core-particle coupling calculation only through a small set of numbers, namely the generalized decoupling factors (11)–(16) and the energies  $\varepsilon_v$ . If one wishes to compare different types of potentials, these are the interesting numbers.

The basis for diagonalizing (10) is obtained by projecting the states  $\chi_\nu$  into states of good total angular momentum. In the present work we will be restricted to the case where all odd intrinsic multipole moments are zero. Then the basis functions must be symmetrized under  $D_2$  symmetry and belong to the representation <sup>22</sup>)  $r_1 = r_2 = r_3$ , i.e.

$$\psi_{MK}^{\nu} = \sum_{\alpha j \Omega} c_{\alpha j \Omega}^{(\nu)} \{ D_{MK}^I \psi_{\Omega}^{2j} + (-)^{I-j} D_{M-K}^I \psi_{-\Omega}^{2j} \} \sqrt{\frac{2I+1}{16\pi^2}}. \quad (17)$$

The summation above is restricted by the fact that  $K - \Omega$  must be an even integer

number. This can then be exploited to restrict both  $K$  and  $\Omega$  to the set of values  $\dots -\frac{3}{2}, \frac{1}{2}, \frac{5}{2} \dots$ . The matrix elements of (10) are easily evaluated in the basis (17). It should be recalled that  $I_+$  and  $I_-$  refer to the intrinsic system and are therefore lowering and raising operators respectively with respect to the index  $K$  on the  $D$ -functions, furthermore that there are additional contributions to the matrix elements from  $K = \frac{1}{2}$  to  $K' = \frac{1}{2}$  and  $-\frac{3}{2}$  due to the symmetrization. Finally, diagonalization gives eigenenergies and eigenstates. The quantities used in the applications below to describe the electromagnetic properties of these states are defined in the appendix.

For the description of the single-particle orbitals we employ the modified oscillator model and obtain the expansion (8) of  $\chi_v$  in coupled harmonic oscillator wave functions referring to a stretched coordinate system<sup>9, 24</sup>).

For small deformations, the difference between a stretched and a non-stretched basis can be ignored. A correct treatment at larger deformation is described in the appendix. In fact, shape isomeric bands at very large deformations are expected to exist in many of the lightest and heaviest nuclei of the periodic table [see e.g. refs. <sup>23, 25, 26</sup>]. Even with other single-particle models than the modified oscillator, it is a commonly used technique to calculate the wave functions on which such bands can be built in terms of stretched oscillator basis functions.

The parameters entering at this stage are the strength parameters  $\kappa$  and  $\mu$  of the  $I \cdot s$  and  $I^2$  terms, and the multipole moments of the core field represented by the deformation parameters  $\varepsilon, \gamma, \varepsilon_{40}, \varepsilon_{42}, \varepsilon_{44}, \dots$  of the single-particle potential in the intrinsic system. Some exploration of the present model as applied to the isotopes <sup>193, 195, 197</sup>Au has already been made in collaboration with Vieu *et al.*, and is presented in ref. <sup>20</sup>).

Pairing is introduced via a standard BCS calculation on the adiabatic single-particle levels. Therefore, the Fermi level  $\lambda_F$  and the pairing occupation factors  $u_v$  and  $v_v$  are uniquely determined without the appearance of additional adjustable parameters. A pairing factor  $u_\mu u_v + v_\mu v_v$  is then attached to each single-particle matrix element, and also the single-particle energies  $\varepsilon_v$  are replaced by quasiparticle energies  $E_v$ . The special character of the recoil term and the blocking effects are ignored. It is well known from the axially symmetric case that agreement with experiment can generally be improved by introducing an *ad hoc* "Coriolis attenuation" parameter. In this work it is denoted  $\xi$  and is multiplied onto the pairing factors.

A more schematic treatment of pairing is used in ref. <sup>20</sup>) and in subsect. 3.3. It only involves the replacement of the single-particle energies  $\varepsilon_v$  by quasiparticle energies calculated with a gap parameter  $\Delta = 12/\sqrt{A}$  MeV and the Fermi level on the orbital occupied by the odd nucleon.

Finally, let us make some comments concerning the determination of the remaining parameters. Potential-energy calculations based on the adiabatic single-particle levels should give indications concerning the multipole moments, but they cannot be used to pin-point for example the effective  $\gamma$ -value in a transitional or axially symmetric nucleus. Under the assumption (7) concerning the rigid rotor

moments of inertia there exist some analytical relationships between measurable core properties and the deformation parameters <sup>4</sup>). Thus  $\gamma$  can be derived from the ratio between the excitation energies of the second and first  $2^+$  states and thereafter  $\varepsilon$  from  $B(E2; 0^+ \rightarrow 2^+)$  and the free moment-of-inertia parameter  $J_0$  from the excitation energy  $E(2^+)$  of the core. Of course the ultimate and often very sensitive test of the parameters lies in the comparison of calculated and experimental properties of the odd- $A$  nucleus.

### 3. Applications

The particle-rotor approach has been a useful implement to nuclear physics for the past twenty-five years. A few special features of the formulation developed in subject. 2.3 above will be illustrated by detailed studies of:

- (i) The positive-parity hole spectrum of the axially symmetric nucleus  $^{185}\text{Re}$ , where the strong-coupling regime prevails. A complete description is obtained after assigning physically reasonable values to the model parameters.
- (ii) The full spectra of the odd-neutron nuclei  $^{75,77}\text{Se}$ , which have not been accounted for in earlier theoretical work. They seem to lie in an oblate-prolate shape transitional region.
- (iii) Certain theoretical aspects of the decoupling of a high- $j$  particle from a transitional core.

#### 3.1. THE NUCLEUS $^{185}\text{Re}$

Fig. 3 shows a modified-oscillator single-particle spectrum that is useful for interpreting the properties of odd-proton nuclei from  $_{75}\text{Re}$  through  $_{81}\text{Tl}$ . There are many indications that a gradual prolate-oblate shape transition takes place over this range in  $Z$ , with maximum triaxiality at  $Z = 79$  for the lighter isotopes and  $Z = 77$  for the heavier ones. Extensive calculations are being undertaken in collaboration with Vieu *et al.* <sup>20</sup>) but lie beyond the scope of the present paper. Here we will merely demonstrate the viability of the model by reproducing all low-lying bands belonging to the positive-parity hole spectrum of the nucleus  $^{185}\text{Re}$ , situated at the outskirts of the transitional region.

The adiabatic single-particle orbitals are calculated with standard “ $A = 187$ ” MO parameters <sup>27</sup>) and six positive-parity orbitals below the prolate  $Z = 76$  gap are included in the coupling calculation. The parameters of the  $^{186}\text{Os}$  core are known from calculations <sup>28</sup>) and experiment to be approximately  $\varepsilon = 0.20$ ,  $\varepsilon_4 = 0.06$ ,  $\gamma = 16^\circ$ ,  $E(2^+) = 137$  keV. However, a fit to the quadrupole moment of the  $^{185}\text{Re}$  ground state, the moment of inertia of the ground band and the position of the  $[411\frac{1}{2}]$  band head indicate that the proton hole polarizes the core significantly, and the parameters actually used are  $\varepsilon = 0.25$ ,  $\varepsilon_4 = 0.08$ ,  $\gamma = 15^\circ$ ,  $E(2^+) = 115$  keV. No Coriolis attenuation was introduced ( $\xi = 1$ ).

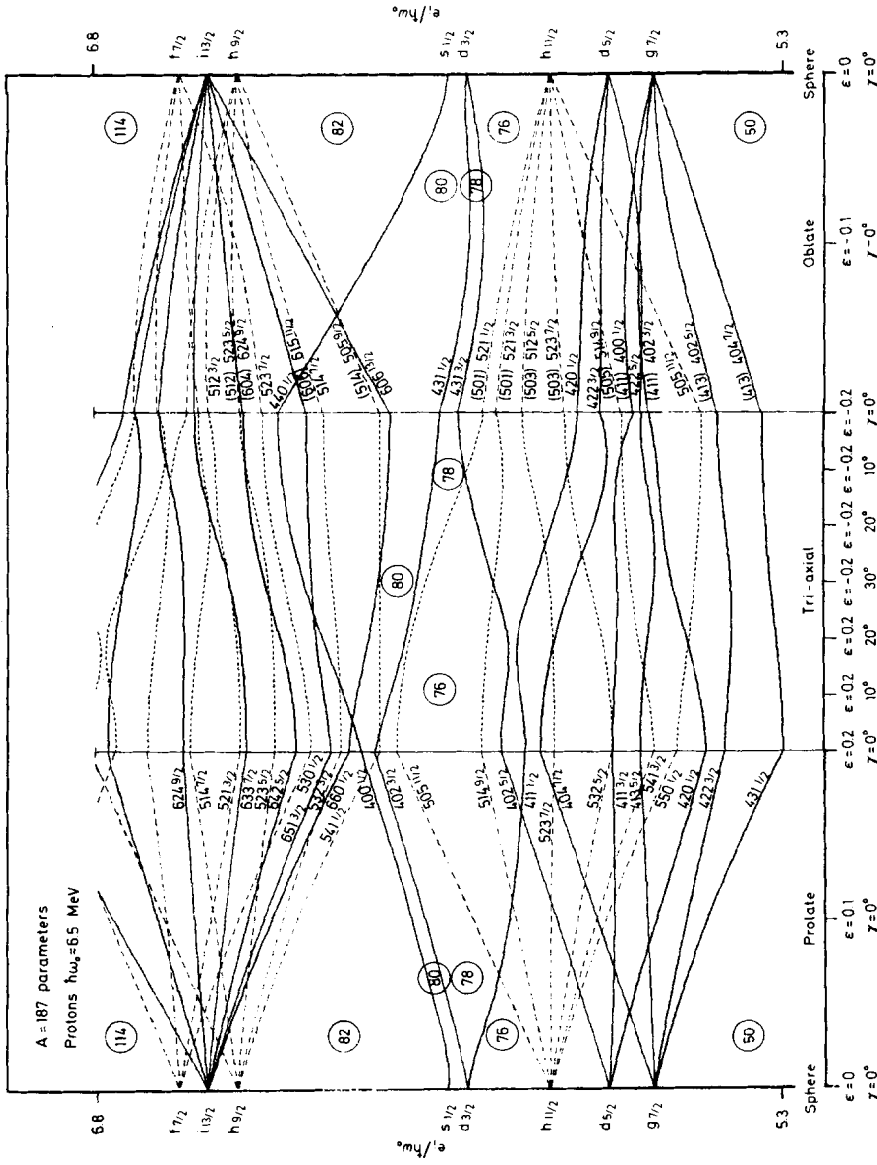


Fig. 3. Adiabatic single-particle orbitals for protons as given by the " $A=187$ " modified oscillator parameters. The orbitals at the left edge and the right edge are identical and correspond to a spherical shape. In between,  $\epsilon$  and  $\gamma$  are varied in such a way that the left part of the figure is drawn for prolate shapes and  $\epsilon$ -values up to 0.2, the middle part shows the orbitals for triaxial shape and in the right part of the figure the orbitals corresponding to oblate shape are exhibited.

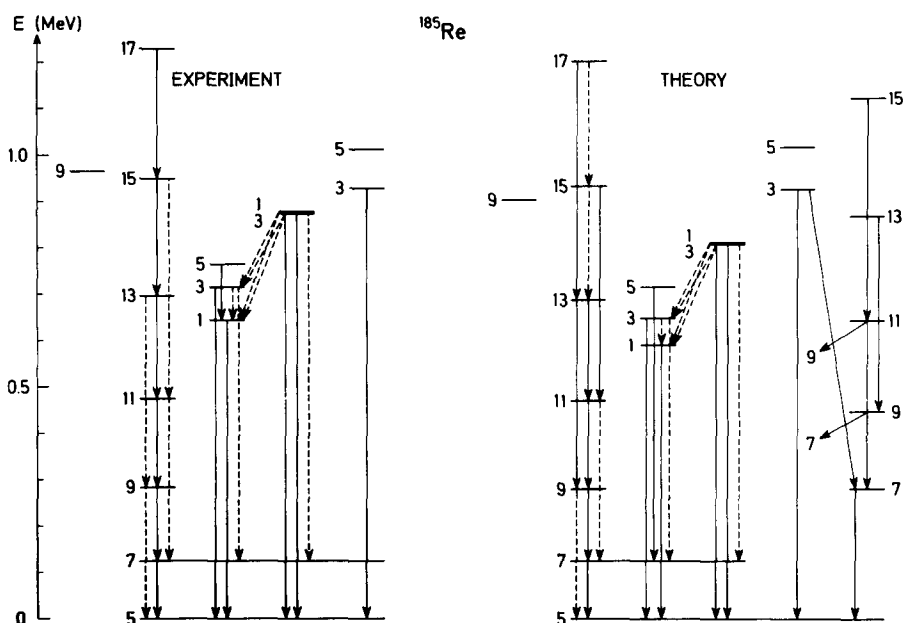


Fig. 4. Experimental and calculated positive-parity hole spectra and  $\gamma$ -decay schemes for the nucleus  $^{185}\text{Re}$ . The calculated spectrum was obtained with the following parameters:  $\epsilon = 0.25$ ,  $\epsilon_4 = 0.08$ ,  $\gamma = 15^\circ$ ,  $E(2^+) = 115$  keV. Apart from the absence of the  $\frac{7}{2}^+$  band in the experimental spectrum, the agreement is quite good.

TABLE 2  
Experimental and calculated electromagnetic properties of the nucleus  $^{185}\text{Re}$

	Theory	Exp.
$Q(e \cdot b)$ $\frac{5}{2}^+$	2.30	2.36
$\mu(\text{n.m.})$ $\frac{5}{2}^+$	2.86	3.17
$B(E2)_1$ $\frac{7}{2}^+$ $\frac{9}{2}^+$ $\frac{11}{2}^+$ $\frac{13}{2}^+$ $\frac{5}{2}^+$ $\frac{7}{2}^+$ $\frac{9}{2}^+$	1.9 0.68 0.032 0.025 0.006 0.054	2.0 0.7 0.03 0.03 0.08
$\delta$ $\frac{7}{2}^+ \rightarrow \frac{5}{2}^+$ $\frac{9}{2}^+ \rightarrow \frac{7}{2}^+$	0.23 0.22	0.19 0.14

The results of the coupling calculation are shown and compared with experiment <sup>29)</sup> in fig. 4 and table 2. The main experimental features are reproduced, although there is still room for improvement by a detailed adjustment of the calculational parameters (e.g.  $\gamma = 14.7^\circ$ ,  $E(2^+) = 115.5$  keV). The three bands indicated to the left in the theoretical spectrum of fig. 4 are mainly based on the orbital  $[402\frac{3}{2}]$  of fig. 3, with predominant  $K$ -quantum numbers equal to the band head spins. The  $\frac{3}{2}^+$ ,  $\frac{1}{2}^+$  doublet stems from the orbital  $[411\frac{1}{2}]$ . The last two bands are built on  $[404\frac{7}{2}]$ , and the lower of them with predominant  $K = \frac{7}{2}$  is not seen experimentally. One possible cause for this is suggested by the calculation, namely strong M1 side-feeding into the ground band which could deplete the intensity of the cascade and in particular the population of the  $\frac{7}{2}^+$  band head. Bands built on the  $[411\frac{3}{2}]$  and  $[413\frac{5}{2}]$  orbitals appear in the theoretical spectrum at 2.4 MeV. In the lower bands, it is only the high-spin states that receive a few percent admixture from these orbitals (see subsect. 3.3.1).

### 3.2. THE NUCLEI <sup>75,77</sup>Se

The excitation spectra of nuclei with mass numbers  $A = 70-80$  appear to lie beyond the scope of all present theories, and a continued investigation gives promise of new developments in the understanding of nuclear systems. Of interest here is the role played by the quadrupole mode. The deformation potentials for the different selenium isotopes, that we obtained from a model described in ref. <sup>30)</sup>, indicate a varying and complex structure.

The potential surface of the  $N = Z$  nucleus <sup>68</sup>Se<sub>34</sub> has two minima of approximately the same depth: a prolate one at  $\epsilon = 0.2$  and an oblate one at  $\epsilon = 0.3$ , separated by a 2 MeV high barrier in the  $\gamma$ -plane. This is an unusual situation, qualitatively similar to what is calculated for <sup>28</sup>Si [ref. <sup>23)</sup>]. The height of the barrier may be overestimated, since pairing is not taken into account for reasons discussed in ref. <sup>30)</sup>. At slightly larger neutron numbers the oblate shell structure is found to dominate, as first predicted in refs. <sup>31,32)</sup>, and in <sup>74,76</sup>Se there is in addition some shell structure at a somewhat larger deformation ( $\epsilon \approx 0.35$ ) and  $\gamma \approx 30^\circ$ . The potential-energy surface for <sup>78</sup>Se is almost completely  $\gamma$ -unstable, and the heavier isotopes have prolate minima at deformations that decrease to zero as the magic neutron number 50 is approached. A similar oblate-prolate transition, taking place at slightly lower neutron number, has also emerged from a Hartree-Fock calculation based on the Skyrme III force <sup>33)</sup>. The recently measured static quadrupole moments in the lowest  $2^+$  states of <sup>76,78,80,82</sup>Se [refs. <sup>34,35)</sup>] are almost independent of neutron number and therefore may imply increasing prolateness to compensate for an assumed decrease in absolute deformation nearer the neutron number 50.

Earlier Coriolis coupling calculations have been taken to indicate prolate deformations in all the Se isotopes <sup>36-38)</sup>. However, extensive experimental information has now become available for the critical nuclei <sup>75,77</sup>Se [see refs. <sup>38-43)</sup> and work quoted therein], and the theoretical spectra cannot be brought into overall

agreement with experiment for any axially symmetric shape of the core. By applying the axially asymmetric Coriolis coupling model of subsect. 2.3 to these two nuclei we may therefore hope to gain some physical insight, and certainly it is interesting to test the model in a region of nuclei whose theoretical description is difficult in many ways. The parameters have been chosen as follows.

The deformed single-particle levels are obtained with the  $A = 70$  parameters of ref. <sup>30</sup>). The BCS calculation includes  $\sqrt{5N}$  levels above and below the Fermi level  $\lambda_F$  and the pairing strength,

$$GA(p) = 22.0 \pm 8.0 \frac{N-Z}{A} \text{ MeV}, \quad (18)$$

is adjusted so that the gap parameter  $\Delta$  on the average equals  $12/\sqrt{A}$  MeV. After an initial survey of deformation space the coordinate  $\varepsilon$  was assigned to be 0.29, close to the values deduced from  $B(E2)$  measurements,  $(p, p')$  scattering data <sup>44</sup>) and the theoretical potential-energy surfaces, while  $\varepsilon_4$  was set equal to zero. The inertial parameter of eq. (7) was adjusted to reproduce the observed spacings of the first few excited states in the odd- $A$  ground bands. The single-particle space spans the orbitals nearest to the Fermi level, five with positive parity and four with negative parity.

The positive-parity spectrum is not very sensitive to  $\gamma$  since the Fermi surface is located near the middle of the  $g_{7/2}$  shell. Instead the requirement of a reasonably good ordering and spacing among the three or four lowest negative-parity levels gives a rather precise determination of  $\gamma$ , viz.  $\gamma = 35^\circ$  for  $^{75}\text{Se}$  and  $\gamma = 30^\circ$  for  $^{77}\text{Se}$ . These  $\gamma$ -values are also used to calculate the positive-parity spectrum. Some "Coriolis attenuation" must then be introduced in the positive-parity Hamiltonian of  $^{75}\text{Se}$  ( $\xi = 0.85$ ) in order to reproduce the  $\frac{5}{2}^+$  ground state. In all the other cases  $\xi$  was set equal to 1.

The calculated results are presented in figs. 5 and 6 and tables 3 and 4 together with the experimental data. There is an overall agreement of non-trivial character. For example, in  $^{77}\text{Se}$  two negative-parity bands appear and the ground-state magnetic moment is adequately reproduced, and for both nuclei the known low-spin states of positive parity occur in the correct order.

Before proceeding with a more detailed analysis it will be instructive to take a closer look at the composition of the single-particle orbitals included in the calculation. Their energies are shown together with the position of the Fermi level in the middle of figs. 5 and 6. More complete single-particle diagrams are available in figs. 2c and 7 of ref. <sup>30</sup>). In terms of a "prolate" basis  $|lj\Omega\rangle$ , where  $\Omega$  is quantized along the major intrinsic axis, the four lower positive-parity orbitals contain between 62 % and 82 % of  $|g_{7/2} \frac{1}{2}\rangle$ ,  $|g_{7/2} \frac{3}{2}\rangle$ ,  $|g_{7/2} \frac{5}{2}\rangle$  and  $|g_{7/2} \frac{7}{2}\rangle$ , respectively, i.e. they are the first four levels of the  $g_{7/2}$  shell. However the fifth  $g_{7/2}$  level lies higher, and the fifth orbital included has an  $\Omega = \frac{1}{2}$  content of 86 %.

In the negative-parity orbitals the  $p_{3/2}$ ,  $f_{7/2}$  and  $p_{1/2}$  shells mix strongly. The three

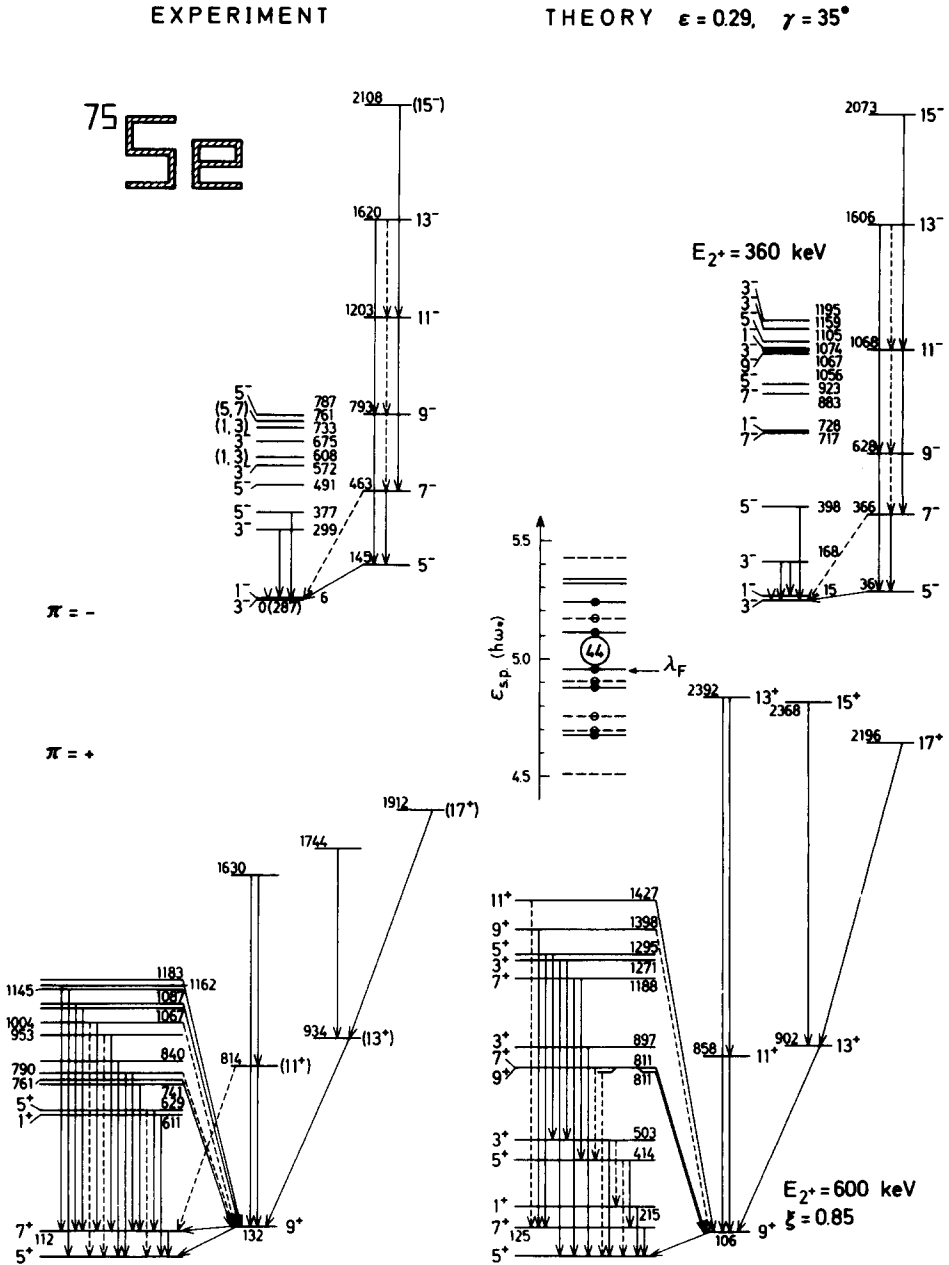


Fig. 5. Experimental and calculated positive- and negative-parity spectra for the nucleus  $^{75}\text{Se}$ . The calculational parameters  $\epsilon$  and  $\gamma$  refer to both negative and positive parity, while the moment of inertia parameter (denoted  $E_2$  in the figure, see subsect. 2.3) and the Coriolis quenching factor  $\xi$  are different for the two parities.  $\xi$  is indicated only in the case where it is not equal to unity. In the middle of the figure the adiabatic single-particle spectrum is shown, with dashed lines for negative-parity orbitals and full lines for positive-parity orbitals [see also ref. <sup>30</sup>]. Orbitals included in the coupling calculation are marked by circles.



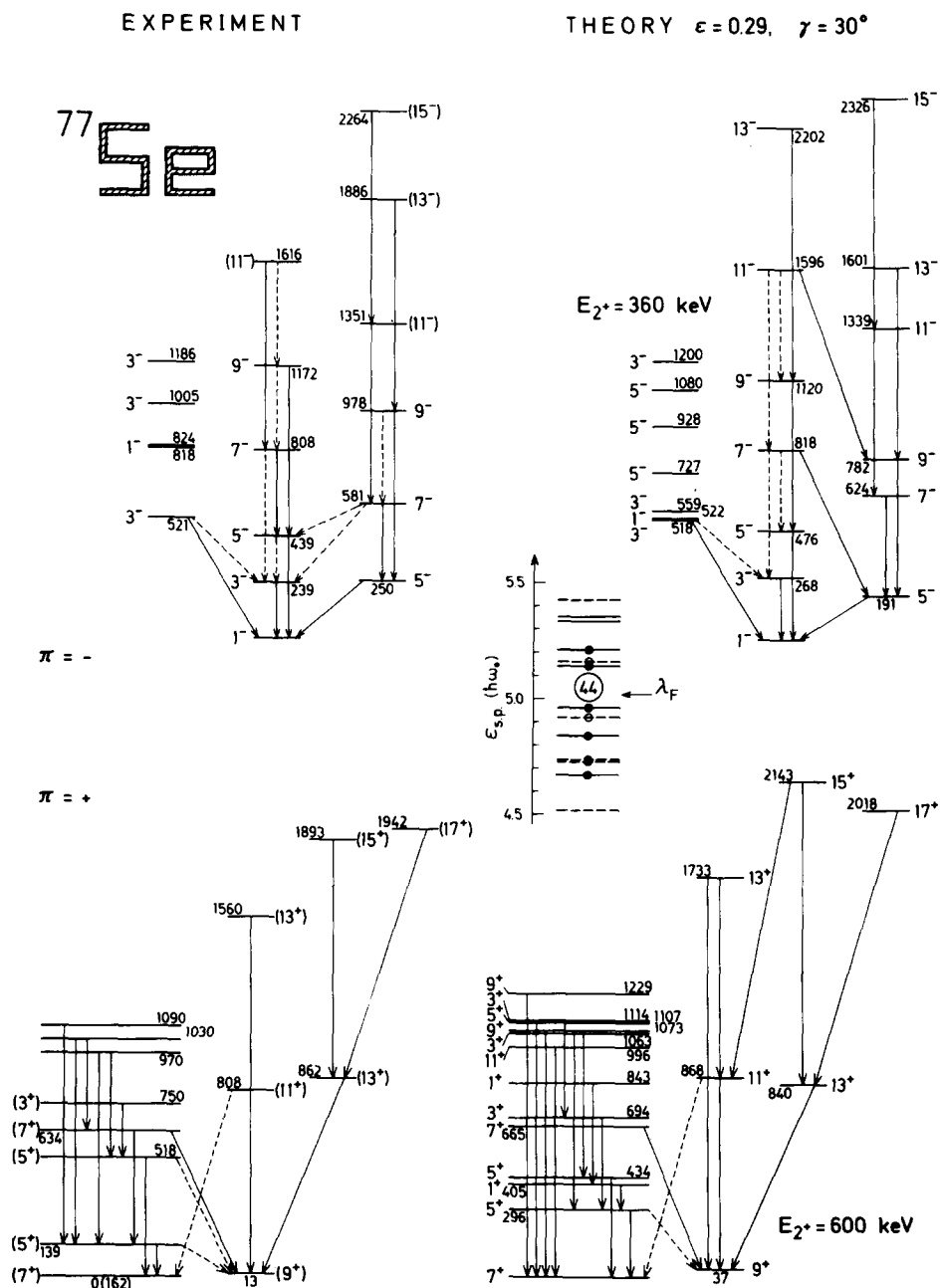
Fig. 6. Same as fig. 5, but for the nucleus  $^{77}\text{Se}$ .

TABLE 3  
Experimental and calculated electromagnetic properties of the nucleus  $^{75}\text{Se}$

$^{75}\text{Se}$	Exp.	Theory
<i>moments</i>		
$\frac{5}{2}^+$	$Q = 1\text{b}$ $\mu = + \text{ or } -0.67 \text{ n.m.}$	$0.02 \text{ b}$ $-1.12 \text{ n.m.}$
<i>half-lives (ns)</i>		
$\frac{1}{2}^-$	30	2600
$\frac{7}{2}^+$	0.69	0.26
$\frac{9}{2}^+$	5.3	21
<i>mixing ratios <math>\delta</math></i>		
$\frac{5}{2}^- \rightarrow \frac{3}{2}^-$	$0.19 \pm 0.10$	0.16
$\frac{7}{2}^- \rightarrow \frac{5}{2}^-$	$0.9 \pm 0.7$	0.8
$\frac{5}{2}^- \rightarrow \frac{3}{2}^-$	$0.73 \pm 0.45$	0.23
<i>branching ratios</i>		
$\frac{9}{2}^- \rightarrow \frac{7}{2}^- / \frac{5}{2}^-$	0.35	0.12
$\frac{11}{2}^- \rightarrow \frac{9}{2}^- / \frac{7}{2}^-$	0.16	0.04
$\frac{13}{2}^- \rightarrow \frac{11}{2}^- / \frac{9}{2}^-$	0.19	0.06
$\frac{3}{2}^- \rightarrow \frac{1}{2}^- / \frac{5}{2}^-$	0.12	2.7
$\frac{5}{2}^- \rightarrow \frac{3}{2}^- / \frac{7}{2}^-$	0.33	0.37
$\frac{11}{2}^+ \rightarrow \frac{9}{2}^+ / \frac{7}{2}^+$	0.64	0.81
$\frac{13}{2}^+ \rightarrow \frac{11}{2}^+ / \frac{9}{2}^+$	0.75	0.34
$\frac{5}{2}^+ \rightarrow \frac{3}{2}^+ / \frac{7}{2}^+$	0.31	0.38
$\frac{5}{2}^+ \rightarrow \frac{3}{2}^+ / \frac{7}{2}^+$	0.06	0.00
<i>E2 rates (W.u.)</i>		
$\frac{7}{2}^+ \rightarrow \frac{5}{2}^+$	125	6
$\frac{9}{2}^+ \rightarrow \frac{7}{2}^+$	34	37
<i>M1 rates (W.u.)</i>		
$\frac{7}{2}^+ \rightarrow \frac{5}{2}^+$	0.02	0.06
$\frac{9}{2}^+ \rightarrow \frac{7}{2}^+$	0.03	0.00

The calculated half-lives and branching ratios do not take into account internal conversion or other modes than M1 and E2. They are based on the experimentally observed transition energies.

upper levels used in the calculation contain approximately 50 % of  $|f_{\frac{5}{2}\frac{1}{2}}\rangle$ ,  $|f_{\frac{3}{2}\frac{1}{2}}\rangle$  and  $|p_{\frac{1}{2}\frac{1}{2}}\rangle$ , respectively. The next higher level comes from the  $h_{\frac{7}{2}}\rangle$  shell, and since  $\epsilon_4$  is taken to be zero the particle-rotor Hamiltonian does not couple it to the other orbitals.

The theoretical positive-parity spectrum of  $^{77}\text{Se}$  is mainly constructed from the three middle levels of the  $g_{\frac{7}{2}}\rangle$  shell, and both the level energies and the decay scheme come close to experiment. The low-lying second  $\frac{1}{2}^+$  state is to be expected when there is a low-lying second  $2^+$  state of the core. The wave function of the theoretical  $\frac{1}{2}^+$  level has a 56 % content of the extraneous fifth single-particle orbital, and therefore the predicted energy of 405 keV has a large uncertainty. In  $^{75}\text{Se}$  this orbital lies

TABLE 4  
Same as table 3, but for the nucleus  $^{77}\text{Se}$

$^{77}\text{Se}$	Exp	Theory
<i>magnetic moment (n.m.)</i>		
$\frac{1}{2}^-$	0.533	0.394
<i>half-lives (ps)</i>		
$\frac{3}{2}^-$	$17 \pm 6$	11
$\frac{5}{2}^-$	$9500 \pm 400$	2150
$\frac{7}{2}^-$	$22 \pm 1.5$	55
$\frac{9}{2}^-$	$7 \pm 5$	45
<i>mixing ratios <math>\delta</math></i>		
$\frac{3}{2}^- \rightarrow \frac{1}{2}^-$	$0.16 \pm 0.05$	0.09
$\frac{5}{2}^- \rightarrow \frac{3}{2}^-$	$0.09 \pm 0.03$	0.57
$\frac{7}{2}^- \rightarrow \frac{5}{2}^-$	$0.12 \pm 0.05$	0.06
$\frac{9}{2}^- \rightarrow \frac{7}{2}^-$	0.17 or 1.2	1.9
$\frac{3}{2}^- \rightarrow \frac{5}{2}^-$	$-0.12 \pm 0.04$	-0.25
$\frac{5}{2}^- \rightarrow \frac{7}{2}^-$	$0.30 \pm 0.06$	0.50
$\frac{7}{2}^- \rightarrow \frac{9}{2}^-$	0.16 or -2.6	0.07
$\frac{1}{2}^- \rightarrow \frac{3}{2}^-$	0.17 or -2.7	0.42
<i>branching ratios</i>		
$\frac{7}{2}^- \rightarrow \frac{3}{2}^- / \frac{5}{2}^-$	0.12	0.00
$\frac{7}{2}^- \rightarrow \frac{5}{2}^- / \frac{9}{2}^-$	0.06	0.06
$\frac{9}{2}^- \rightarrow \frac{7}{2}^- / \frac{5}{2}^-$	< 0.33	0.03
$\frac{5}{2}^- \rightarrow \frac{3}{2}^- / \frac{1}{2}^-$	0.80	0.00
$\frac{7}{2}^- \rightarrow \frac{5}{2}^- / \frac{9}{2}^-$	0.50	0.47
$\frac{9}{2}^- \rightarrow \frac{7}{2}^- / \frac{5}{2}^-$	0.21	0.00
$\frac{11}{2}^- \rightarrow \frac{9}{2}^- / \frac{7}{2}^-$	0.11	0.26
$\frac{3}{2}^- \rightarrow \frac{5}{2}^- / \frac{1}{2}^-$	0.10	0.87
$\frac{5}{2}^- \rightarrow \frac{7}{2}^- / \frac{3}{2}^-$	0.014	0.18
$\frac{7}{2}^- \rightarrow \frac{9}{2}^- / \frac{5}{2}^-$	0.001	0.06
$\frac{5}{2}^+ \rightarrow \frac{7}{2}^+ / \frac{3}{2}^+$	0.12	0.02
$\frac{7}{2}^+ \rightarrow \frac{9}{2}^+ / \frac{5}{2}^+$	0.04	0.00
$\frac{9}{2}^+ \rightarrow \frac{7}{2}^+ / \frac{5}{2}^+$	0.06	0.12
<i>E2 rates (W.u.)</i>		
$\frac{3}{2}^- \rightarrow \frac{1}{2}^-$	45	28
$\frac{5}{2}^- \rightarrow \frac{3}{2}^-$	2	13
$\frac{7}{2}^- \rightarrow \frac{5}{2}^-$	45	29
$\frac{5}{2}^- \rightarrow \frac{3}{2}^-$	< 18	2
$\frac{7}{2}^- \rightarrow \frac{5}{2}^-$	4	6
$\frac{9}{2}^- \rightarrow \frac{7}{2}^-$	5	8
$\frac{7}{2}^- \rightarrow \frac{5}{2}^-$	5	7
$\frac{9}{2}^- \rightarrow \frac{7}{2}^-$	2	5
<i>M1 rates (W.u.)</i>		
$\frac{3}{2}^- \rightarrow \frac{1}{2}^-$	0.095	0.140
$\frac{5}{2}^- \rightarrow \frac{3}{2}^-$	0.053	0.000
$\frac{7}{2}^- \rightarrow \frac{5}{2}^-$	0.020	0.001
$\frac{9}{2}^- \rightarrow \frac{7}{2}^-$	0.013	0.008
$\frac{7}{2}^- \rightarrow \frac{5}{2}^-$	0.002	0.002

further from the Fermi surface and does not affect the low-energy levels. The positions of the high-spin states of  $^{75}\text{Se}$  reflect a larger discrepancy than in  $^{77}\text{Se}$  between the experimental and the rigid rotor core spectra – at the  $\gamma$ -values employed and under the assumption of eq. (7).

The low-energy negative-parity spectrum of  $^{75}\text{Se}$  is mainly built on the third orbital, leading to correct branching and mixing ratios along the yrast line. The decay properties of the other low-lying states are not so well described. The fourth orbital gives rise to the second  $\frac{1}{2}^-$  state, and the second orbital to the doublet calculated at  $\approx 1070$  keV. In  $^{77}\text{Se}$  the two negative-parity bands arise from a strong mixing between orbitals 3 and 4 across the Fermi surface. Only the two  $\frac{1}{2}^-$  states are almost purely 4 and 3, respectively. Thus the odd particle has a large  $p_{\frac{3}{2}}$  component in the ground state, which is consistent with the measured spectroscopic factor<sup>45</sup>). Up to the first  $\frac{7}{2}^-$  level the electromagnetic properties are described well considering the complexity of the wave functions. At higher energies a peculiar situation arises with one possible band classification based on the E2 decay of the core as shown in fig. 6, and another based on the predominant single-particle parentage. In the latter case the band memberships of the two  $\frac{9}{2}^-$  states are interchanged and likewise for the  $\frac{13}{2}^-$  states. However, the near degeneracy of the  $R \pm \frac{1}{2}$  states characteristic of a  $p_{\frac{3}{2}}$  spectrum are not seen in experiment, neither are the strong M1 transitions predicted to take place between the “E2 bands”.

Let us focus attention on some weak points in the calculation.

(i) The level density in the experimental spectrum of  $^{75}\text{Se}$  increases sharply at about 600 keV, earlier than in the theoretical level scheme. This may partly be ascribed to the influence of the first excited  $0^+$  state, which is absent in the theoretical core but is seen experimentally at the anomalously low energy 854 keV in the  $N = 40$  isotope  $^{74}\text{Se}$ . Generally, if there are additional low-lying states with small quadrupole matrix elements connecting to the ground- and  $\gamma$ -bands, they will give rise to a second family of odd- $A$  levels bearing similarities to the first family and interacting with it only weakly. Whether or not this is the case here, it is clear that the restriction to a rigid rotor core can be a severe limitation in the study of states that are far from yrast.

(ii) Electromagnetic properties are on the whole only roughly reproduced. With regard to the M1 properties, this may be partly due to the schematically evaluated  $g$ -factors.

(iii) The negative-parity band structure in  $^{77}\text{Se}$  is also only roughly reproduced, as was pointed out above. Possibly a major source of difficulty for the model lies in band mixing across the Fermi surface.

(iv) The moment-of-inertia parameter for the negative-parity bands corresponds to a 360 keV excitation energy in the first  $2^+$  state of the core, far below the experimentally observed values 633, 560 and 614 keV in  $^{74, 76, 78}\text{Se}$ , respectively. In contrast the positive-parity states  $\frac{11}{2}^+$  and  $\frac{13}{2}^+$  are reproduced at about 800 keV above the  $\frac{9}{2}^+$  state with a parameter value corresponding to 600 keV, i.e. precisely the average of the experimental  $2^+$  energies. The large contribution to the moment of inertia from

an odd negative-parity particle cannot be easily understood as a pure deformation effect in the present case. If it is due to a lesser degree of superfluidity in the negative-parity states, which the present model is not designed to be able to take into account, then the underlying mechanism is still unclear to us. Certainly a general structural difference between the negative- and positive-parity odd- $A$  states lies in the amount of spreading over different single-particle orbitals, which is larger for the high- $j$  positive-parity states. However, the positive-parity orbitals 2, 3 and 4 primarily involved lie quite close to the Fermi level, and the blocking of these orbitals would therefore influence the pairing solution as much as the negative-parity orbitals 3 or 4.

(v) The energy separation of the lowest positive- and negative-parity odd- $A$  states may also be interpreted to indicate weaker pairing for negative parity. The calculation, which assumes the same gap parameter  $\Delta$  for both parities, depresses the negative-parity spectrum by 485 keV in  $^{75}\text{Se}$  and 413 keV in  $^{77}\text{Se}$ , relative to experiment.

(vi) The  $\frac{5}{2}^+$  state in  $^{75}\text{Se}$  was obtained as the lowest positive-parity level only after an *ad hoc* manipulation amounting to a quenching of the Coriolis term ( $\xi = 0.85$ ) that is frequently used in the literature but inadequately justified by theory. Moreover, the wave functions of the lowest states cannot be considered satisfactory. Although many of the experimental decay data involving these states are reproduced, there is a particularly large discrepancy for the  $B(E2; \frac{7}{2}^+ \rightarrow \frac{5}{2}^+)$  value. Also there is considerable deviation from the experimental ground-state quadrupole moment, which, however, is not completely reliable <sup>46)</sup>.

To summarize the discussion of points (iii)–(vi), it is possible that a refined treatment of pairing would be a major improvement of the model.

Some effects that are neglected here are blocking, higher multipoles of the pairing force [see e.g. ref. <sup>47)</sup>], coupling between particle and hole states <sup>8)</sup> and coupling to many-quasiparticle configurations.

### 3.3. HIGH- $j$ INTRUDER SHELLS

**3.3.1. Rotational alignment.** When the odd particle occupies high- $j$  orbitals different band structures may arise that are characteristic of specific angular momentum coupling schemes. These are quite well understood both at large, intermediate and small core deformations <sup>3, 48–51)</sup>. The cases of large and intermediate deformations will be reviewed here in the language of the strong coupling representation. This gives insight into the transition between the two regions of deformation and clarifies the causes for changes in the odd- $A$  spectrum engendered by hexadecapole deformation or an additional single-particle  $j$ -shell, as will be studied in the following sections.

Let us consider the simple case of a rigid, axially symmetric core with the inertial parameter equal to unity. The Hamiltonian is then

$$H = R^2 + \sum_{\Omega} \delta_{\Omega\Omega'} \varepsilon_{\Omega'} = I^2 + j^2 - 2I \cdot j + \sum_{\Omega} \delta_{\Omega\Omega'} \varepsilon_{\Omega'} \quad (19)$$

The deformed field of the core splits the adiabatic single-particle orbitals into pairs of time-reversed orbitals  $|\pm\Omega\rangle$ , and in the adiabatic approximation the lowest eigenstates of  $H$  are built exclusively on the pair closest to the Fermi surface. However, the Coriolis term  $-2\mathbf{I} \cdot \mathbf{j}$  mixes in components from other orbitals. Physically this can be viewed as a tendency toward alignment of the particle spin  $\mathbf{j}$  with  $\mathbf{I}$ , equivalent to alignment or in some cases antialignment between  $\mathbf{j}$  and the core spin  $\mathbf{R}$ , in order to minimize the Coriolis energy. This corresponds to a decoupling of the particle motion from that of the core, and the adiabatic approximation ceases to be valid. The alignment effect is weak if the adiabatic single-particle orbitals are well separated in energy, e.g. due to a large quadrupole deformation. It is also weak if the orbitals closest to the Fermi surface have large projections on the symmetry axis, since such orbitals are not very useful for constructing states aligned along a perpendicular axis of rotation. Without alignment a normal rotational band develops with spin sequence  $I = \Omega, \Omega+1, \dots$ . A unique position is held by orbitals with  $\Omega = \pm\frac{1}{2}$  and thus minimal projection on the symmetry axis. From them it is possible to construct semialigned states without spreading the wave function over any other single-particle orbitals. One way of understanding this is to consider the particle restricted to a space spanned by  $|+\frac{1}{2}\rangle$  and  $|-\frac{1}{2}\rangle$  and then to crank the core field. Diagonalization of the cranking Hamiltonian gives two states  $\sqrt{\frac{1}{2}}(|\frac{1}{2}\rangle \pm |-\frac{1}{2}\rangle)$  with average projections of  $j$  on the rotation axis amounting to  $\pm\frac{1}{2}(j+\frac{1}{2})$ , respectively. The factor  $\frac{1}{2}$  motivates the description of such states as semialigned. They are eigenstates of  $e^{i\pi j_x}$  and thus the symmetry which leads to the absence of odd-spin states in the core is not broken in the core-plus-particle system. Therefore the aligned states can only have spins  $\dots, j-2, j, j+2, \dots$ . The eigenvalues of  $H$  are roughly equal to

$$I^2 + j^2 \mp Ij + \varepsilon_{\frac{1}{2}} \quad (20)$$

for the partially aligned and antialigned states, respectively.

Let us now consider the effect of the non-adiabatic “spreading” over several single-particle orbitals. When the Fermi level is near the  $\Omega = \frac{1}{2}$  orbital, the inherent semialignment is improved by such spreading and approaches full alignment. Then the energies of the odd-mass system are approximately

$$I^2 + j^2 \mp 2Ij + \sum_{\Omega} |c_{\Omega}|^2 \varepsilon_{\Omega}. \quad (21)$$

Compared to the adiabatic case, it is clear that the aligned states of large  $I$  are depressed more than the aligned states of small  $I$ , while the energies of the anti-aligned states come much higher. In fact, the so-called unfavoured states of a fully decoupled band are not antialigned but almost aligned states, built on two or more single-particle orbitals situated further from the Fermi level.

So far we have limited our discussion to axially symmetric nuclei in which case the collective rotation can only take place around a perpendicular axis and the moment of inertia is fixed. For triaxial nuclei the situation is similar but more

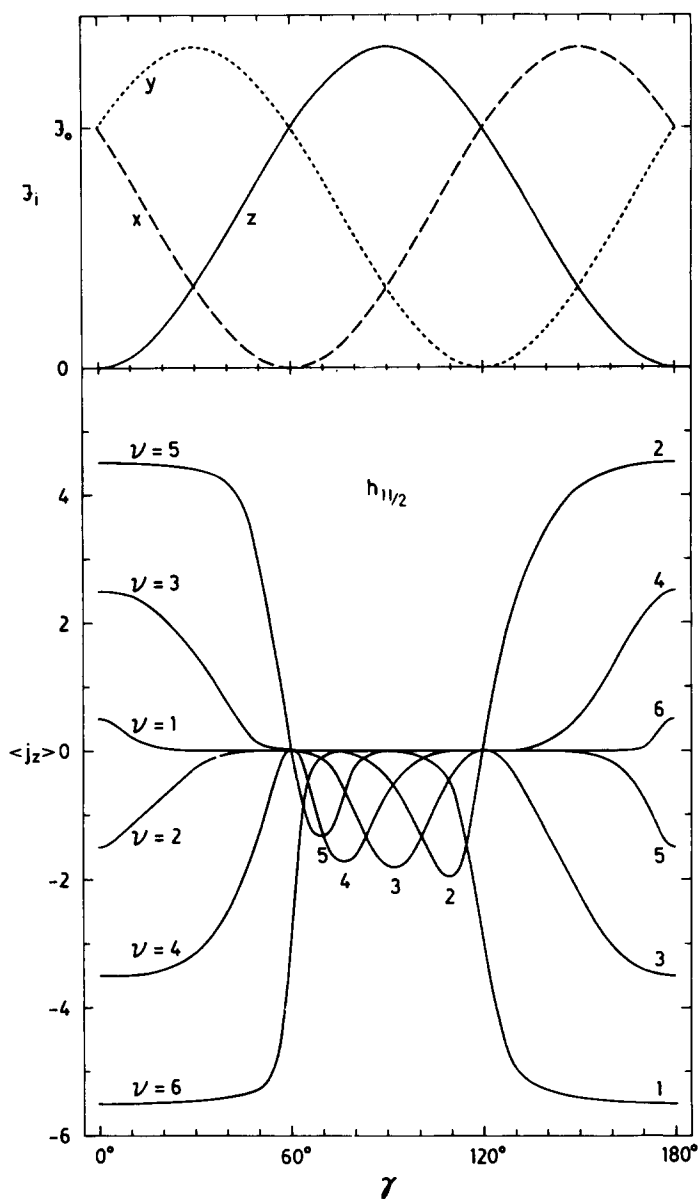


Fig. 7. In the lower part of the figure, the expectation values of  $j_z$  for the  $h_{11/2}$  shell orbitals at  $\epsilon = 0.16$  are shown as a function of  $\gamma$ . The orbitals are labelled in order of increasing energy ( $\nu = 1, 2, \dots, 6$ ). For  $\gamma = 0^\circ$  and  $120^\circ$  the nucleus is prolate, while it is oblate for  $\gamma = 180^\circ$  and  $60^\circ$ . The  $z$ -axis is the symmetry axis for  $\gamma = 0^\circ$  and  $180^\circ$  and a perpendicular axis for  $\gamma = 120^\circ$  and  $60^\circ$ . Note that for those orbitals which have a large spin component on the symmetry axis for oblate and prolate shape (respectively,  $\gamma = 0^\circ$  and  $180^\circ$ ) this component remains rather unchanged far out in the  $\gamma$ -plane. In the upper part of the figure the variation with  $\gamma$  of the hydrodynamical moments of inertia is illustrated.

complex. Partly, the complexity comes from the fact that all three moments of inertia are different from zero which means that the collective rotation can take place around an arbitrary axis. Thus if we allow  $\gamma$  to vary between  $0^\circ$  and  $60^\circ$  we should, to get a complete description, study all three axis,  $x$ ,  $y$  and  $z$ . Equivalently, we can allow  $\gamma$  to vary over  $180^\circ$  and concentrate on one axis. Fig. 7 is drawn in this way with  $\gamma$  varying from  $0^\circ$  to  $180^\circ$ . In the lower part of the figure, the expectation values of  $j_z$  are shown. It is interesting to note that starting from prolate shape at  $0^\circ$  the three orbitals highest in energy remain almost pure  $j_z = \frac{11}{2}$ ,  $\frac{9}{2}$  and  $\frac{7}{2}$  states up to full triaxiality at  $30^\circ$ . A similar but less pronounced situation holds if we start for oblate shape at  $180^\circ$ ; the two lower orbitals remain almost pure  $j_z = \frac{11}{2}$  and  $\frac{9}{2}$  up to  $150^\circ$ , which value of  $\gamma$  corresponds to the same shape as  $\gamma = 30^\circ$ .

As these states have large components of  $j_z$  in the mentioned regions of  $\gamma$ , they are not very useful to construct states with a large spin component in a perpendicular direction.

The part of fig. 7 that carries most information about decoupling is the region between  $60^\circ$  and  $120^\circ$ . The reason is that  $J_z$  is the larger moment of inertia as can be

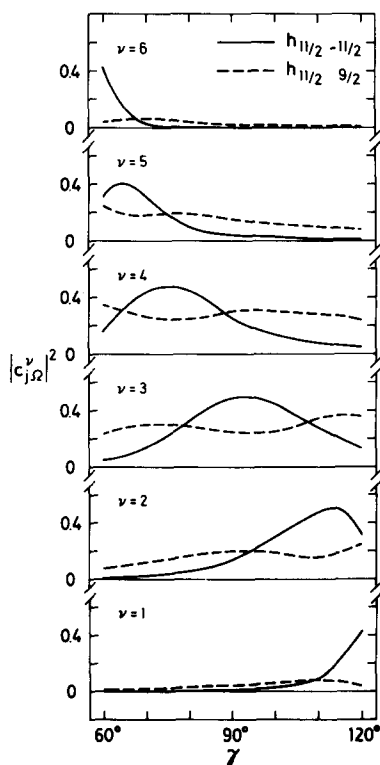


Fig. 8. The amplitudes of the  $j_z = -\frac{11}{2}$  and  $\frac{9}{2}$  components of the  $h_{11/2}$  shell are illustrated as a function of  $\gamma$ . The range in  $\gamma$  is  $60^\circ$ – $120^\circ$ , which is the region where  $J_z$  is the largest of the three moments of inertia.

As in fig. 7, the label  $\nu$  refers to the energy ordering of the subshell orbitals.



seen in the upper part of fig. 7. In this region of  $\gamma$  it is energetically favourable for the collective rotation to take place around the  $z$ -axis. For the high-spin yrast states the Coriolis term will then try to align the single-particle angular momentum with that of the rotor and for the formation of yrast states of high spin the important question is how single-particle states with large values of  $j_z$  could be formed in this region of  $\gamma$  (for axial shapes, see also ref. <sup>50</sup>). This can partly be seen from the expectation values of  $j_z$  in fig. 7 but is better illustrated in fig. 8 where the amplitudes of the components with  $j_z = -\frac{11}{2}$  and  $\frac{9}{2}$  are plotted for the different single-particle orbitals. The conclusion is that starting from oblate shape at  $\gamma = 60^\circ$  it is mainly the upper orbitals ( $v = 5, 6$ ) that build the  $j_z = -\frac{11}{2}$  state, continuing over  $80^\circ$  this state is mainly built from orbitals 3 and 4, at  $90^\circ$  from orbitals 2, 3 and 4, at  $100^\circ$  from orbitals 2 and 3 for prolate shape at  $120^\circ$  from orbitals 1 and 2. As concerns the amplitudes of the  $j_z = \frac{9}{2}$  state they are mainly distributed over orbitals 2, 3, 4 and 5 with a tendency towards the upper orbitals close to oblate shape and a tendency towards the lower orbitals close to prolate shape. This is probably part of the mechanism behind the well-known “ $(j-1)$  effect” in the middle of the shell. Although the  $j_z = \frac{9}{2}$  component in orbitals 2 and 5 is not very large around  $\gamma = 90^\circ$ , it is certainly much larger than the  $\frac{11}{2}$  component and due to the moment of inertia effect, this component can be expected to be important in addition to the much larger component of  $j_z = \frac{9}{2}$  of orbitals 2 and 5 at  $\gamma \approx 150^\circ$  and  $30^\circ$ , respectively.

TABLE 5

The occupation probabilities of the six adiabatic single-particle orbitals originating from the  $h_{11/2}$  shell in selected states of an odd-mass nucleus with the Fermi level on the lowest orbital

$\gamma$ (deg)	Level	s.p. orbital					
		1	2	3	4	5	6
0	$\frac{11}{2}_1$	45	34	16	4	0	0
0	$\frac{23}{2}_1$	43	33	17	6	1	0
0	$\frac{13}{2}_1$	4	29	39	22	5	0
0	$\frac{21}{2}_1$	4	27	38	24	7	1
0	$\frac{11}{2}_2$	22	0	21	39	17	2
30	$\frac{11}{2}_1$	76	18	4	1	0	0
30	$\frac{23}{2}_1$	24	33	30	11	2	0
30	$\frac{13}{2}_1$	63	27	7	3	1	0
30	$\frac{21}{2}_1$	51	34	10	4	1	0
30	$\frac{11}{2}_2$	30	30	29	10	1	0
60	$\frac{11}{2}_1$	83	15	2	0	0	0
60	$\frac{23}{2}_1$	15	25	22	16	12	10
60	$\frac{13}{2}_1$	68	25	6	1	0	0
60	$\frac{21}{2}_1$	29	36	22	10	3	0
60	$\frac{11}{2}_2$	14	37	30	12	5	2

The single-particle orbitals are numbered in order of increasing energy. The core parameters are  $\epsilon = 0.16$ ,  $\gamma = 0^\circ, 30^\circ$  or  $60^\circ$  and 300 keV excitation energy for the first  $2^+$  state.

It is now easy to understand the wave functions for the particle states at different values of  $\gamma$  as illustrated in table 5. Starting at prolate shape ( $\gamma = 0^\circ$  or  $\gamma = 120^\circ$ ) we find that the  $\frac{1}{2}$  state is spread over the low-lying orbitals so as to form a state with maximal spin projection ( $\frac{1}{2}$ ) on the perpendicular axis. The favoured band is then built by adding the parallel core angular momentum which is seen by the fact that the  $\frac{23}{2}$  state has a single-particle distribution almost identical to that of the  $\frac{1}{2}$  state. In a similar way the structure of the unfavoured band is very stable with the same single-particle distribution in the  $\frac{13}{2}$  state as in the  $\frac{21}{2}$  state. These states can be approximately described as formed from a single-particle state with spin projection  $\frac{5}{2}$  on the perpendicular axis<sup>50</sup>).

For  $\gamma = 30^\circ$  the  $\frac{1}{2}$  state is built from the low-lying orbitals due to the single-particle term. However, with increasing spin the Coriolis term becomes more important and we noticed above that the single-particle state with maximal spin projection on the axis of largest moment of inertia is built from single-particle orbitals in the middle of the shell. Thus, with increasing spin, the single-particle distribution moves to the middle of the shell. Similar effects, although less drastic, are noticed in the unfavoured band.

On the oblate side, the  $\frac{1}{2}$  state starts out as a strong coupled one, however with a noticeable contribution also from the  $\Omega = \frac{5}{2}$  orbital. It is also interesting to note that the spreading increases quite a lot with increasing spin and that the  $\frac{23}{2}$  state has an almost equal distribution over all levels. This spreading has the effect that the energy spacing between the states is smaller and increases slower than in a normal rotational band. As concerns the second  $\frac{1}{2}$  state also shown in table 6, we notice that in all cases it is not adiabatic at all but is spread over several single-particle orbitals.

Generally, there will be a tendency due to the single-particle term that the favoured band starts out as built from states close to the Fermi surface but with increasing spin tends to be built from the lower states for prolate shape, from the states in the middle of the shell for triaxial shape and from states in the upper part of the shell for oblate shape.

So far we have just fixed the deformation and calculated the rotational bands. The discussion above leads, however, to the conclusion that for the favoured yrast band there will be a trend relative to the  $\frac{1}{2}$  state toward prolate shape for particle states, towards  $\gamma = 30^\circ$  if we are in the middle of the shell and towards oblate shape for hole states (see fig. 10 below). In addition the  $\gamma$ -dependence of the moment of inertia has a tendency to polarise the nucleus. With the moments of inertia of hydrodynamical type this effect will drive towards  $\gamma = 30^\circ$  (or equivalently  $90^\circ$ ) where the largest moment of inertia is maximal (fig. 7).

The figs. 7 and 8 are rather independent of the deformation  $\varepsilon$  while the mixing over different single-particle orbitals, given for  $\varepsilon = 0.16$  in table 5, is certainly strongly dependent on  $\varepsilon$ . The reason is that when the levels come further apart with increasing  $\varepsilon$ , the energy cost to distribute a state over several single-particle orbitals is higher.

The distance between the single-particle orbitals also depends on the location in

the shell and the  $\gamma$ -value (see fig. 3 above). Thus, for axial shape, the orbitals with a large spin projection on the symmetry axis are much further apart than those with a small spin projection. For  $\gamma$  around  $30^\circ$ , the orbitals are more evenly distributed, however with some concentration in the middle of the shell [for a realistic test case of the adiabatic approximation at  $\gamma \approx 30^\circ$ , see ref. <sup>20</sup>]. The energy distribution of the orbitals of the shell also depends on other deformation coordinates, for example  $\varepsilon_4$ , and on the mixing with other shells as discussed in the following sections.

Especially at larger deformations, it is interesting to ask what kind of alignment could be achieved without spreading the wave function over several orbitals. This was discussed above at axial symmetry for  $\Omega = \frac{1}{2}$  states. The semi-alignment of the single-particle spin, which is equal to  $\pm \frac{1}{2} (j + \frac{1}{2})$ , can be directly seen in fig. 7 as the expectation value of  $j_z$  for orbitals 6 and 1 at  $\gamma = 60^\circ$  and  $120^\circ$ , respectively. However, the large slope of  $\langle j_z \rangle$  at these two points indicates that the semialignment is very sensitive to  $\gamma$ . Furthermore, studying the amplitudes of  $\langle j_z \rangle$  in fig. 7 between  $\gamma = 60^\circ$  and  $120^\circ$ , we notice that it is different orbitals which can be partly aligned along the axis of largest moment of inertia. Thus, while it is orbital 1 at prolate shape, it is mainly orbital 2 for  $\gamma = 10^\circ$  ( $110^\circ$ ), orbital 3 for  $\gamma = 30^\circ$ , orbital 4 for  $\gamma = 40^\circ$ , orbital 5 for  $\gamma = 50^\circ$  and of course only orbital 6 for  $\gamma = 60^\circ$ . It is also seen that the partial alignment in the respective triaxial orbitals cannot become as large as the semialignment in axial orbitals.

**3.3.2. Hexadecapole deformation.** The higher multipoles in eq. (2) have been completely ignored in earlier core-particle coupling calculations, with a few exceptions such as ref. <sup>52</sup>). However many nuclei in different parts of the periodic table are predicted to have significant ground-state hexadecapole moments, and in some cases there is concurrent evidence from analyses of scattering and Coulomb interference data. An intrinsic hexadecapole moment alters the wave functions of the adiabatic orbitals entering the coupling calculation and changes their relative energies. An example of its effect on odd- $A$  electromagnetic properties when the orbitals have low  $j$ -values can be studied in ref. <sup>20</sup>). In a decoupled band, built on a high- $j$  intruder shell, hexadecapole deformation can change the relative positions of the favoured and unfavoured states. This was first noted by Baker and Goss <sup>53</sup>), who were able to reproduce parts of the  $h_{\frac{7}{2}}$  particle spectrum of  $^{187}\text{Ir}$  without any  $\gamma$ -deformation in the prolate core, but including the diagonal contributions to the adiabatic orbitals from a very large negative hexadecapole moment.

Here this result will be clarified and extended by studying the effect of  $\varepsilon_4$  on high- $j$  particle spectra for  $\gamma = 0^\circ, 30^\circ$  and  $60^\circ$ . There are actually three independent intrinsic hexadecapole coordinates, but a  $\gamma$ -dependent linear combination has been chosen that reduces to  $\varepsilon_{40}$  along the respective symmetry axes for  $\gamma = 0^\circ$  and  $60^\circ$  [ref. <sup>30</sup>]]. It should be recalled that a positive value of  $\varepsilon_{40}$  corresponds to a negative hexadecapole moment <sup>54</sup>). The lowest  $h_{\frac{7}{2}}$  shell is used for the model study, so the parameters  $\kappa, \mu, \varepsilon$  and  $J_0$  are assigned values characteristic of nuclei in the  $A \approx 130$  region.

The lower part of fig. 9 exhibits the  $\varepsilon_4$  dependence of the adiabatic  $h_{\frac{7}{2}}$  single-

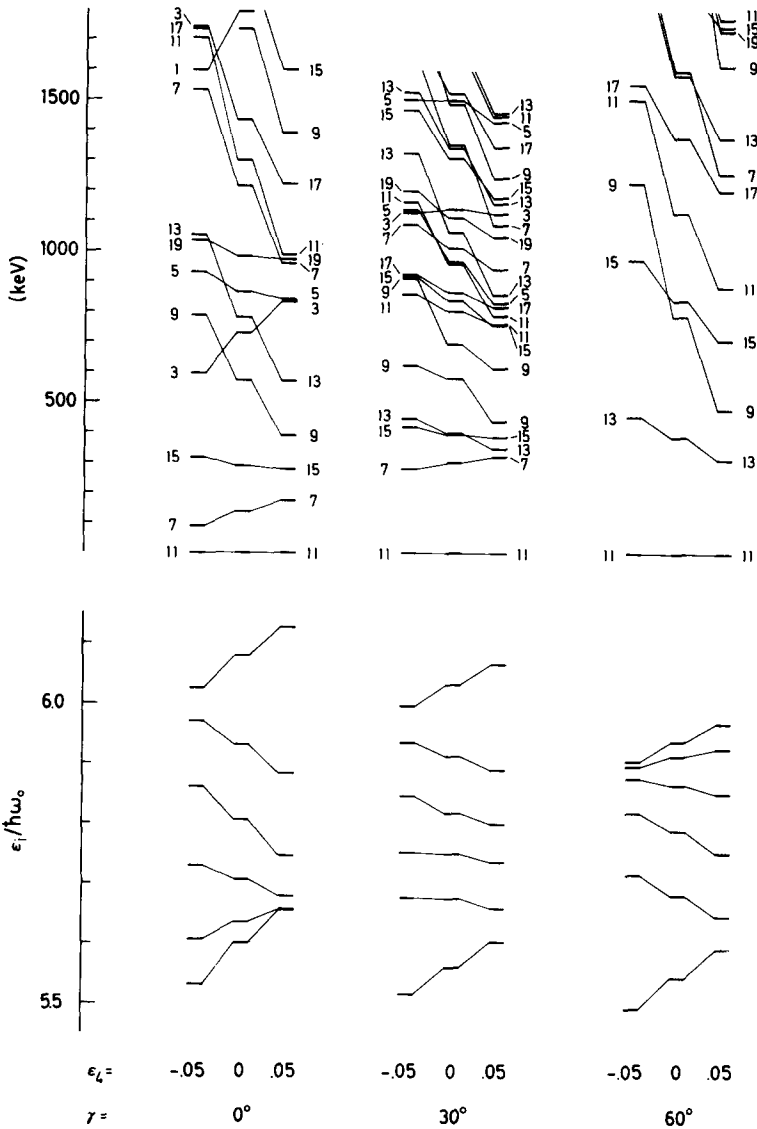


Fig. 9. The lower part of the figure shows adiabatic single-particle spectra of orbitals with predominantly  $h_{11/2}$  content, calculated at  $\epsilon = 0.16$  and different values of  $\epsilon_4$  and  $\gamma$ . The MO parameters are  $\kappa = 0.0620$ ,  $\mu = 0.614$ , appropriate for protons in the  $A = 130$  region. The upper part gives the odd- $A$  spectra obtained when a particle free to occupy these orbitals is coupled to a rotational core with  $E(2^+) = 0.3$  MeV.

particle energies. The diagonal contributions from  $\epsilon_4$ , solely responsible for the effect studied in ref. <sup>53</sup>), can reproduce the trends qualitatively but not quantitatively. The slight compression of the oblate spectrum compared to the prolate one is mainly due to the presence of the  $f_{7/2}$  shell (fig. 3) and will be further commented in the next section. The fundamental feature shown in fig. 9 is that, for all  $\gamma$ -values, the value of

$\varepsilon_4$  strongly affects the energy separation of the lowest orbitals, which are the most important ones when the Fermi level is assumed to lie below the shell. From this fact, and from the results of subsect. 3.3.1, it is straightforward to interpret the changes in the odd- $A$  particle spectra shown in the upper part of fig. 9.

In the decoupled  $\gamma = 0^\circ$  band the favoured states are primarily built on the lowest  $\Omega = \frac{1}{2}$  orbital, while the main components of the unfavoured states come from the next two orbitals. Therefore the unfavoured states come down when  $\varepsilon_4$  is increased, as would also happen if a  $\gamma$ -deformation was introduced but for a different reason. The low-spin favoured states  $\frac{7}{2}^-$  and  $\frac{3}{2}^-$  are never fully decoupled because they can only utilize orbitals with  $\Omega \leq I$ , and thus move up relative to the others since the high-spin states draw greater advantage from the compression of almost all the orbitals.

In the strong coupled  $\gamma = 60^\circ$  case the separation of the two lowest orbitals largely determines the separation of the  $K = \frac{11}{2}$  and  $K = \frac{9}{2}$  bands. As mentioned in subsect. 3.3.1 there is greater spreading over the orbitals at higher spins in order to minimize the increasingly important Coriolis term. When the lowest orbitals come closer together this spreading is facilitated and the effect on the spectrum is an increase of the effective moment of inertia, clearly emerging in fig. 9. For  $\gamma = 30^\circ$  the energies of the yrast states do not depend sensitively on  $\varepsilon_4$ .

Finally, it should be mentioned that the position of the BCS Fermi level is stable against the displacement of a few individual levels. If it for example lies slightly above the first  $h_{1/2}$  orbital at  $\varepsilon_4 = 0$ , then the quasiparticle energies will vary only weakly with  $\varepsilon_4$  and the effects shown in fig. 9 will be damped. In fig. 9 the Fermi level is consistently placed on the lowest orbital, and quasiparticle energies are calculated assuming a gap parameter  $\Delta = 12/\sqrt{A}$  MeV.

*3.3.3. The effect of  $j$ -mixing.* In high- $j$  intruder shells at small deformations the  $j$ -mixing is small, but even then it has a non-negligible influence on both the high- and the low-spin states of the odd- $A$  spectrum [ref. <sup>15</sup>) and fig. 2 above]. Here we will see how the underlying mechanism can be understood from the point of view of the strong-coupling basis approach.

Again  $h_{1/2}$  particle states will be selected for study. In order to establish the nature of the influence from the  $f_{7/2}$  shell, a particle is coupled to a  $\beta$ -deformed,  $\gamma$ -unstable core with parameters that could be characteristic for a nucleus like  $^{126}\text{Xe}$ . The method of ref. <sup>7</sup>) is used, which for this case essentially implies an intermediate coupling calculation where the full core space is taken into account. The particle space is restricted first to the  $h_{1/2}$  shell and then to the  $h_{1/2}$  and  $f_{7/2}$  shells with an energy separation of 5 MeV. The two resulting odd- $A$  spectra are compared in fig. 10, where it is seen that the inclusion of the  $f_{7/2}$  shell has an effect similar to the addition of a term proportional to  $-\cos 3\gamma$  in the core potential <sup>7</sup>). The inference, that  $f_{7/2}$  single-particle components tend to polarize the core towards the prolate side, is confirmed by the plot in fig. 10 showing the quantities  $\langle \cos 3\gamma \rangle$  for the core in some yrast states of the odd- $A$  system. The mechanism is schematically illustrated in the upper right-hand part of

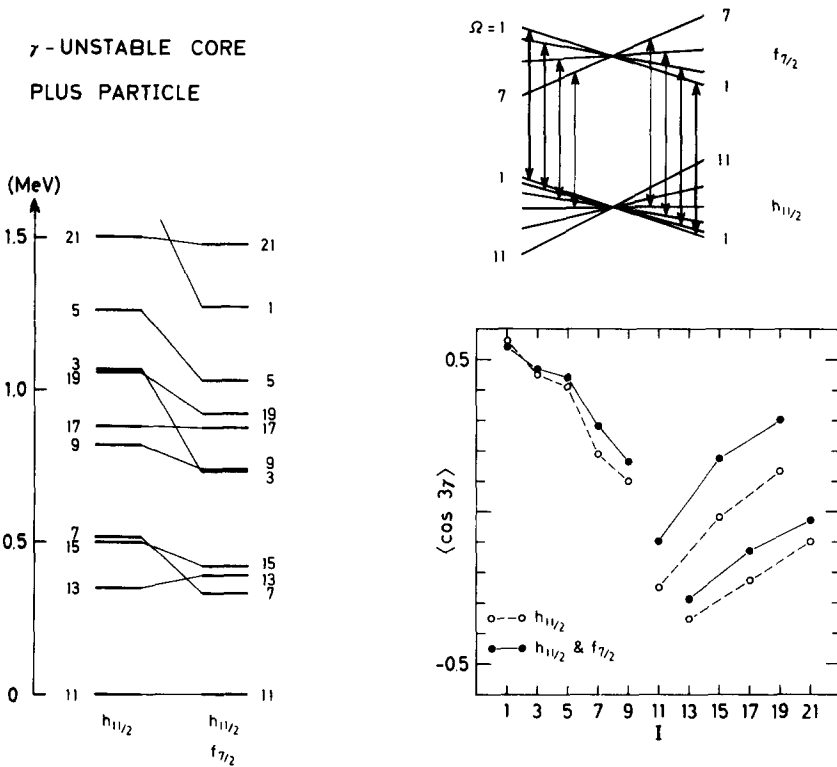


Fig. 10. A particle is coupled to a  $\beta$ -deformed,  $\gamma$ -unstable core with and without the inclusion of the  $f_{7/2}$  shell at an energy of 5 MeV above the  $h_{11/2}$  shell. In the lower left part the effects are shown on the odd- $A$  energy spectrum and in the lower right part the effects on the average intrinsic deformation of the core in yrast states of the odd- $A$  system are exhibited. In this figure, a value of  $\langle \cos 3\gamma \rangle$  which is larger than zero corresponds to a tendency towards prolate shape while for  $\langle \cos 3\gamma \rangle < 0$  there is a tendency towards oblate shape. The upper right-hand part of the figure schematically illustrates the deformation-induced couplings between the adiabatic single-particle levels.

fig. 10, depicting the adiabatic single-particle levels at oblate ( $\epsilon < 0$ ) and prolate ( $\epsilon > 0$ ) shapes and also the deformation-induced couplings between them. Because of the  $\Omega$ -selection rule for axially symmetric deformations, the lowest  $h_{1/2}$  orbitals are depressed by couplings to  $f_{3/2}$  orbitals on the prolate but not on the oblate side. Thus, with only the  $h_{1/2}$  shell included, the high-spin states are more oblate and closer to the strong coupling limit while with the  $f_{3/2}$  shell included, these states come closer to the decoupled limit characteristic of particle states for prolate shape.

A rigid core cannot be polarized. Nevertheless, with a predominantly prolate core ( $\gamma < 30^\circ$ ), the inclusion of the  $f_{3/2}$  shell leads to similar changes in the odd- $A$  spectrum<sup>6)</sup> because the levels that are built primarily on the lowest – and the most prolate – single-particle orbital will go down in energy. For example, in the extreme case  $\gamma = 0^\circ$  only the  $f_{3/2}$  and  $h_{1/2}$  orbitals of equal  $\Omega$  interact, with matrix elements propor-

tional to

$$(j - 2\Omega 20|j\Omega) \approx (j^2 - \Omega^2)((j-1)^2 - \Omega^2), \quad j = \frac{11}{2}, \quad (22)$$

i.e. large for small values of  $\Omega$ . Thus the energy differences between the  $\Omega = \frac{1}{2}$  orbital and the higher orbitals of the  $h_{1/2}$  shell are made larger by the interaction with the  $f_{7/2}$  shell. The consequences of this for the odd- $A$  spectrum have already been discussed in the previous section, where a qualitatively similar shift of the orbitals appeared in connection with negative  $\varepsilon_4$  values. The relative energies of the unfavoured odd- $A$  levels increase, despite the fact that an  $f_{7/2}$  admixture to the wave function of the  $\Omega = \frac{1}{2}$  single-particle orbital reduces the decoupling factor.

In the intermediate coupling calculation above, the most important  $j$ -shell in addition to  $h_{1/2}$  could easily be coped with. However, considering the multitude of additional inter-shell couplings that arise between spherical basis states in a deformed potential, numerical convergence cannot be expected at this point. In the approach of subsect. 2.3 all these additional couplings are taken into account in the eigenstates of the deformed single-particle Hamiltonian.

#### 4. Conclusion and discussion

There exists a wide variety of core-quasiparticle coupling models derived from the Bohr Hamiltonian. The aim of this work has been to extract their essential features and to formulate the rudiments of a model that has a maximal range of applicability under the subsidiary requirement of simplicity, i.e. that the parameters be few and directly related to theoretically and experimentally available properties of nuclear many-particle systems. For reasons given in subsects. 2.1 and 2.2 we have chosen to generalize the Hecht-Satchler model by removing the restriction of adiabaticity. The necessary formalism has been provided in subsect. 2.3 and for very large deformations in the appendix. Several ramifications of the basic model are immediately obvious, but for the study of near-yrast states the most promising one may be to include some aligned three-quasiparticle configurations, thereby extending the range of applicability both in nucleon number towards the shell-model nuclei and in spin upward along the yrast line.

The viability of the model in its present form is essentially already established by work with earlier models contained as special cases, but is also demonstrated in a few applications. A calculation for  $^{185}\text{Re}$  may be taken to illuminate the role of the  $g_{7/2}$  levels. A brief exploration was conducted into the poorly understood selenium region, and the wave functions of states based on high- $j$  orbitals were analyzed.

We would like to express our appreciation to S. G. Nilsson for many suggestions, discussions and comments. Valuable comments from R. K. Sheline and Z. Szymański are gratefully acknowledged. We are also indebted to J. S. Dionisio and C. Vieu for many stimulating discussions. This work was supported by the Swedish Atomic Research Council.

### Appendix

The reduced electromagnetic transition rates are defined as

$$B(O\lambda; I_i \rightarrow I_f) = \frac{1}{2I_i + 1} |\langle I_f || \mathcal{M}(O\lambda) || I_i \rangle|^2. \quad (\text{A.1})$$

The mixing ratio  $\delta$  that can be deduced from angular correlation measurements is given by

$$\delta = \sqrt{0.7} E_\gamma \frac{\langle I || \mathcal{M}(E2) || I-1 \rangle}{\langle I || \mathcal{M}(M1) || I-1 \rangle}. \quad (\text{A.2})$$

A simple sign rule states that  $\delta$  is negative for a transition between a favoured state and an unfavoured state in a decoupled band. For the M1 and E2 operators between states expanded in the basis (17), with expansion coefficients  $a_K^{I\nu}$ , we have

$$\begin{aligned} \langle I' || \mathcal{M}(M1) || I \rangle &= \left\{ \frac{3}{4\pi} (2I+1) \right\}^{\frac{1}{2}} \sum_{\substack{KK' \\ \nu\nu'}} a_K^{I'\nu'} a_K^{I\nu} [g_R \delta_{I'I} \delta_{K'K} \delta_{\nu'\nu} \{I(I+1)\}^{\frac{1}{2}} \\ &\quad + \langle IK10 | I'K' \rangle \{ (g_s - g_l) \langle \chi_\nu | s_z | \chi_\nu \rangle + (g_l - g_R) \langle \Omega \rangle_{\nu\nu} \} \\ &\quad + \sqrt{\frac{1}{2}} (-)^{I'-\frac{1}{2}} \langle IK1-1 | I'K' \rangle \{ (g_s - g_l) \langle \chi_{\nu'} | s_+ | \tilde{\chi}_\nu \rangle + (g_l - g_R) (a+b)_{\nu'\nu} \} \\ &\quad + \sqrt{\frac{1}{2}} (-)^{I'+\frac{1}{2}} \langle IK11 | I'K' \rangle \{ (g_s - g_l) \langle \chi_\nu | s_- | \tilde{\chi}_\nu \rangle + (g_l - g_R) c_{\nu'\nu} \}], \quad (\text{A.3}) \end{aligned}$$

$$\begin{aligned} \langle I' || \mathcal{M}(E2) || I \rangle &= \left\{ \frac{5}{16\pi} (2I+1) \right\}^{\frac{1}{2}} \sum_{\substack{KK' \\ \nu\nu'}} a_K^{I'\nu'} a_K^{I\nu} \\ &\quad \times [(Q_0 \delta_{\nu\nu'} + \langle \chi_\nu | \hat{q}_{20} | \chi_\nu \rangle) \langle IK20 | I'K' \rangle \\ &\quad + (Q_2 \delta_{\nu\nu'} + \langle \chi_\nu | \hat{q}_{22} | \chi_\nu \rangle) (\langle IK22 | I'K' \rangle + \langle IK2-2 | I'K' \rangle)]. \quad (\text{A.4}) \end{aligned}$$

For  $g_s$  we use 0.6 times the experimental value for a free nucleon.

The single-particle matrix elements of  $s_z$ ,  $s_+$  and  $s_-$  are most easily calculated after the trivial transformation via Clebsch-Gordon coefficients from the representation (8) to the basis  $|\alpha \frac{1}{2} \Lambda \Sigma\rangle$ . The intrinsic quadrupole moments  $Q_0$  and  $Q_2$  of the core are obtained by summing the single-particle quadrupole moments up to the proton Fermi surface. In calculations for odd-neutron nuclei the proton wave functions are not calculated for any other purpose and it is expedient to use the macroscopic values instead. Expressions for the matrix elements of the single-particle quadrupole operators  $\hat{q}_{2\mu}$  in a stretched basis are given in ref. <sup>23)</sup>.

In order to obtain the generalized decoupling factors in a stretched basis, the spherical orbital angular momentum operators of eqs. (11)–(16) can be written out as differential operators in Cartesian coordinates and explicitly transformed to stretched coordinates. With the index  $l$  to distinguish stretched quantities, the resulting ex-



pressions contain the operator  $l'$  and in addition

$$f_z^t = -i \left( x_t \frac{\partial}{\partial y_t} + y_t \frac{\partial}{\partial x_t} \right) = -\frac{1}{2} [A_t, i x_t y_t], \quad (\text{A.5})$$

$$f_{\pm}^t = \frac{1}{2} [A_t, \pm z_t (x_t \mp i y_t)], \quad (\text{A.6})$$

$$g_{1,2}^t = [A_t, [A_t, z_t^2 (x_t^2 \pm y_t^2)]], \quad (\text{A.7})$$

$$g_3^t = [A_t, [A_t, x_t^2 y_t^2]]. \quad (\text{A.8})$$

These operators are written as commutators and double commutators containing Laplacians because such matrix elements can in an oscillator basis be reduced according to the relations

$$\langle N_t \alpha_t | [A_t, f(\mathbf{r}_t)] | N_t' \alpha_t' \rangle = 2(N_t' - N_t) \langle N_t \alpha_t | f(\mathbf{r}_t) | N_t' \alpha_t' \rangle \quad (\text{A.9})$$

$$\langle N_t \alpha_t | [A_t, [A_t, x_t^\lambda y_t^\mu z_t^\nu]] | N_t' \alpha_t' \rangle = 4 \{ (N_t' - N_t)^2 - (\lambda + \mu + \nu) \} \langle N_t \alpha_t | x_t^\lambda y_t^\mu z_t^\nu | N_t' \alpha_t' \rangle. \quad (\text{A.10})$$

The selection rules in  $N_t$  are clearly exhibited by these equations;  $N_t' = N_t \pm 2$  for the  $f^t$  operators and  $N_t' = N_t, N_t \pm 4$  for the  $g^t$  operators. In the present application  $\alpha_t$  corresponds to a set of stretched angular quantum numbers, most conveniently chosen as  $(l_t A_t \Sigma)$ , and the matrix elements and selection rules for the polynomials are readily obtained after an expansion in  $Y_n^m(\theta_t, \phi_t)$ . The polynomials in  $f_z^t$  and  $f_{\pm}^t$  are proportional to  $(Y_2^2 - Y_2^{-2})$  and  $Y_2^{\mp 1}$ , respectively. The expansion of the polynomial in  $g_1^t$  contains  $Y_0^0, Y_2^0$  and  $Y_4^0$ , the polynomial in  $g_2^t$  has  $(Y_2^2 + Y_2^{-2})$  and  $(Y_4^2 + Y_4^{-2})$ , while  $g_3^t$  gives  $Y_0^0, Y_2^0, Y_4^0$  and  $(Y_4^4 + Y_4^{-4})$ .

More specifically, let us introduce the notation  $\omega_x, \omega_y, \omega_z$  for the oscillator frequencies and furthermore

$$A, B = \frac{1}{2} \left( \sqrt{\frac{\omega_y}{\omega_x}} \pm \sqrt{\frac{\omega_x}{\omega_y}} \right),$$

$$\alpha, \beta, \gamma, \delta = \frac{1}{4} \left( \sqrt{\frac{\omega_z}{\omega_y}} \frac{+}{-} \sqrt{\frac{\omega_y}{\omega_z}} \frac{+}{-} \sqrt{\frac{\omega_x}{\omega_z}} \frac{+}{-} \sqrt{\frac{\omega_z}{\omega_x}} \right), \quad (\text{A.11})$$

where the uppermost set of signs on the right corresponds to the first letter on the left and so forth. The components of the single-particle angular momentum operator  $j$  are obtained as

$$j_z = s_z + A l_z^t + B f_z^t, \quad (\text{A.12})$$

$$j_{\pm} = s_{\pm} + \alpha l_{\pm}^t + \beta l_{\mp}^t + \gamma f_{\pm}^t + \delta f_{\mp}^t. \quad (\text{A.13})$$

From these expressions it is straightforward to obtain also  $j_z^2, j_+^2 + j_-^2$  and  $j_+ j_- + j_- j_+$

in terms of products of two stretched operators. The non-zero matrix elements of such products containing one or no  $f^i$  operators are easily found and written, since there is then a unique intermediate state. The entering products of two  $f^i$  operators can be decomposed as

$$f_+^i f_-^i + f_-^i f_+^i = \frac{1}{3}(l_+^i l_-^i + l_-^i l_+^i) + \frac{8}{3} - \frac{1}{6}g_1^i, \quad (\text{A.14})$$

$$f_+^{i2} + f_-^{i2} = \frac{1}{3}(l_+^{i2} + l_-^{i2}) + \frac{1}{6}g_2^i, \quad (\text{A.15})$$

$$f_z^{i2} = \frac{2}{3} + \frac{1}{3}l_z^{i2} - \frac{1}{12}g_3^i. \quad (\text{A.16})$$

### References

- 1) A. Bohr, Mat. Fys. Medd. Dan. Vid. Selsk. **26**, no. 14 (1952)
- 2) A. Bohr and B. R. Mottelson, Mat. Fys. Medd. Dan. Vid. Selsk. **27**, no. 16 (1953)
- 3) J. Meyer-ter-Vehn, Nucl. Phys. **A249** (1975) 111, 141
- 4) A. S. Davydov and G. F. Filippov, Nucl. Phys. **8** (1958) 237
- 5) V. V. Pashkevich and R. A. Sardaryan, Nucl. Phys. **65** (1965) 401
- 6) A. Faessler and H. Toki, Phys. Lett. **59B** (1975) 211
- 7) G. Leander, Nucl. Phys. **A273** (1976) 286
- 8) F. Dönaue and S. Frauendorf, Phys. Lett. **71B** (1977) 263
- 9) S. G. Nilsson, Mat. Fys. Medd. Dan. Vid. Selsk. **29**, no. 16 (1955)
- 10) K. T. Hecht and G. R. Satchler, Nucl. Phys. **32** (1962) 286
- 11) W. Scholz and F. B. Malik, Phys. Rev. **176** (1968) 1355
- 12) A. Faessler, Nucl. Phys. **59** (1964) 177
- 13) E. Osnes, J. Rekstad and O. K. Gjötterud, Nucl. Phys. **A253** (1975) 45
- 14) T. Yamazaki, Nucl. Phys. **49** (1963) 1; Proc. INS Symp. on nuclear collectivity, Tokyo, 1976, p. 480
- 15) H. Toki and A. Faessler, Nucl. Phys. **A253** (1975) 231
- 16) D. R. Bès, Nucl. Phys. **10** (1959) 373
- 17) I. Y. Lee, D. Cline, P. A. Butler, R. M. Diamond, J. O. Newton, R. S. Simon and F. S. Stephens, Phys. Rev. Lett. **39** (1977) 684
- 18) G. Alaga, Rendiconti SIF, corso XL (NY, 1976) p. 28
- 19) V. Paar, Nuovo Cim. **32A** (1976) 97
- 20) Ch. Vieu, S. E. Larsson, G. Leander, I. Ragnarsson, W. de Wiclawik and J. S. Dionisio, J. of Phys. **G** to be published, and submitted
- 21) A. K. Kerman, Mat. Fys. Medd. Dan. Vid. Selsk. **30**, no. 15 (1956)
- 22) A. Bohr and B. R. Mottelson, Nuclear structure, vol. 2 (Benjamin, Reading, Mass, 1975)
- 23) G. Leander and S. E. Larsson, Nucl. Phys. **A239** (1975) 93
- 24) S. E. Larsson, Physica Scripta **8** (1973) 17
- 25) S. E. Larsson, G. Leander, S. G. Nilsson, I. Ragnarsson and R. K. Sheline, Phys. Lett. **47B** (1973) 422
- 26) P. Möller, Nucl. Phys. **A192** (1972) 529
- 27) S. G. Nilsson, C. F. Tsang, A. Sobiczewski, Z. Szymański, S. Wycech, C. Gustafsson, I.-L. Lamm, P. Möller and B. Nilsson, Nucl. Phys. **A131** (1969) 1
- 28) I. Ragnarsson, A. Sobiczewski, R. K. Sheline, S. E. Larsson and B. Nerlo-Pomorska, Nucl. Phys. **A233** (1974) 329
- 29) Y. A. Ellis, Nucl. Data Sheets **12** (1974) 533
- 30) S. E. Larsson, G. Leander, I. Ragnarsson and G. Alenius, Nucl. Phys. **A261** (1976) 77
- 31) I. Ragnarsson and S. G. Nilsson, Colloque sur les noyaux de transition, Orsay, 1971, p. 112
- 32) F. Dickman, V. Metag and R. Repnow, Phys. Lett. **38B** (1972) 207
- 33) D. Ardouin, R. Tamisier, M. Vergnes, G. Rotbard, J. Kalifa, G. Berrier and B. Grammaticos, Phys. Rev. **C12** (1975) 1745
- 34) R. Lecomte, P. Paradis, J. Barrette, M. Barette, G. Lamoureux and S. Monaro, Nucl. Phys. **A284** (1977) 123
- 35) P. B. Vold, D. Cline, J. Sprinkle and R. Scharenberg, Bull. Amer. Phys. Soc. **21** (1976) 581

- 36) S. L. Heller and J. N. Friedman, Phys. Rev. **C10** (1974) 1509
- 37) N. E. Sanderson, Nucl. Phys. **A216** (1974) 173
- 38) N. E. Sanderson and R. G. Summers-Gill, Nucl. Phys. **A261** (1976) 93
- 39) D. J. Horen and M. B. Lewis, Nucl. Data Sheets **16** (1975) 25
- 40) K. O. Zell, H.-G. Friedrichs, B. Heits, P. von Brentano and C. Protop, Z. Phys. **A272** (1975) 27
- 41) P. P. Urone, L. L. Lee and S. Raman, Nucl. Data Sheets **9** (1973) 229
- 42) R. A. Braga and D. J. Sarantites, Phys. Rev. **C9** (1974) 1493
- 43) K. O. Zell, H.-G. Friedrichs, B. Heits, D. Hippe, H. W. Schuh, P. von Brentano and C. Protop, Z. Phys. **A276** (1976) 371
- 44) E. Hentschel and G. Heinrich, Nucl. Phys. **A144** (1970) 92
- 45) E. K. Lin, Phys. Rev. **139** (1965) B340
- 46) G. H. Fuller and V. W. Cohen, Nucl. Data Sheets, App. 1 (1965)
- 47) I. Hamamoto, Nucl. Phys. **A232** (1974) 445
- 48) A. K. Kerman, Mat. Fys. Medd. Dan. Vid. Selsk. **30**, no. 15 (1956)
- 49) F. S. Stephens, R. M. Diamond, J. R. Leigh, T. Kammuri and K. Nakai, Phys. Rev. Lett. **29** (1972) 438
- 50) F. S. Stephens, R. M. Diamond and S. G. Nilsson, Phys. Lett. **44B** (1973) 429
- 51) P. Vogel, Phys. Lett. **33B** (1970) 400
- 52) A. A. Raduta, V. Ceausescu and R. M. Dreizler, Nucl. Phys. **A272** (1976) 11
- 53) F. T. Baker and D. Goss, Phys. Rev. Lett. **36** (1976) 852
- 54) B. Nilsson, Nucl. Phys. **A129** (1969) 445